submitted to *xxxx*

Revisiting piezoelectric sensor calibration methods using elastodynamic stress waves

Rui Wu[1], Paul Antony Selvadurai[2], Chaojian Chen[3] and Omid Moradian[1]

[1] *Engineering Geology Group, ETH Zürich, Zürich, Switzerland. Email: rui.wu@erdw.ethz.ch*

[2] *Swiss Seismological Service, ETH Zürich, Zürich, Switzerland.*

[3] *Institute of Geophysics, ETH Zürich, Zürich, Switzerland.*

21 September 2020

SUMMARY

The application of absolutely calibrated piezoelectric (PZT) sensors is increasingly used to help interpret the information carried by radiated seismic waves in laboratory and *in situ* seismology. In this paper, we revisit the methodology based on the finite element method (FEM) to characterize PZT sensors. The FEM-based modelling tool is used to numerically compute the Green's function between a ball impact source, and an array of PZT sensors used to detect laboratory-induced elastic stress wave propagation excited by a unit step force-time function. Realistic boundary conditions that capture the experimental conditions, are adopted to physically constrain the problem of elastic wave propagation, reflection and transmission in/on the elastic medium. The modelling methodology is first validated against the reference approach (generalized ray theory) and is then extended down to 1 kHz where elastic wave reflection and transmission along different types of boundaries are explored. We find the Green's functions calculated for realistic boundaries have distinct differences between commonly employed

idealized boundary conditions, especially around the anti-resonant and resonant frequencies. Unlike traditional methods that use singular ball drops, we find that each ball drop is only partially reliable over specific frequency bands. We demonstrate, by adding spectral constraints, that the individual instrumental responses are accurately cropped and linked together over 1 kHz to 1 MHz after which they overlap with little amplitude shift. This study finds that ball impacts with a broad range of diameters as well as the corresponding valid frequency bandwidth and equivalent seismic magnitude, are necessary to characterize broadband PZT sensors from 1 kHz to 1 MHz. This work bridges the gap between microcrack/damage mechanics and laboratory/*in situ* acoustic emissions (AEs) by unraveling sources in terms of the physics that generates AE signals.

Key words: wave propagation; Fourier analysis; numerical modelling; seismic instruments

1 INTRODUCTION

1.1 Application of PZT sensors to AE monitoring

As brittle rocks are subjected to external stress in a laboratory setting, localized and rapid inelastic deformation events occur that are associated with the growth or appearance of small defects at the grain-scale (from microns to millimeters), which can generate acoustic emissions (AEs) (e.g., Lockner 1993; Grosse & Ohtsu 2008; Ishida et al. 2017). These emissions can cause high-frequency vibrations, at frequencies ranging from tens of kHz to several MHz, within rocks and are recorded by piezoelectric (PZT) sensors at known locations. In the last decade, much effort has been made to improve our understanding of laboratory-generated AEs in a quantitative manner (McLaskey & Glaser 2011; McLaskey et al. 2014; Goodfellow 2015; Selvadurai 2019). These studies differ from previous AE studies, in that they characterized the absolute mechanical energy released by fracturing processes due to

the radiated waves in the stressed solids instead of the traditional parametric analysis of the voltage measured by PZT sensors (Moradian et al. 2016).

Fracture-induced seismic stress waves are not limited to the laboratory scale; they are also referred to as induced seismicity, a negative byproduct of engineering activities, such as hydrocarbon storage and extraction, shale gas exploitation, mining operations, and impoundment of water behind dams (Grigoli et al. 2017). To help understand the induced seismicity and manage the induced seismic risk in geoEnergy applications, local down borehole networks of PZT sensors were developed for *in situ* AE monitoring at the decameter scale (Kwiatek et al. 2011, 2017; Manthei & Plenkers 2018; Goodfellow & Young 2014; Zang et al. 2016; Kneafsey et al. 2018; Amann et al. 2018; Schoenball et al. 2019; Villiger et al. 2020). Recently, Villiger et al. (2020) reported on the induced seismicities caused by hydraulic stimulation experiments in a 20 m $\times$ 20 m $\times$ 20 m crystalline rock volume at the Grimsel Test Site, Switzerland. They used calibrated PZT sensors in boreholes surrounding the injection locations and monitored the induced seismic events in a magnitude range from -6.2 to -2.5 over 1 to 50 kHz (Villiger et al. 2020).

1.2 Absolute characterization of PZT sensors

Recent advances in both laboratory and *in situ* AE monitoring during fracturing experiments has greatly improved our understanding of microcrack mechanisms over broadband ranges of source dimension and frequency. Prior to exploring such seismic characteristics, it is essential to absolutely characterize the PZT sensors utilized in both laboratory and *in situ* applications so that the information conveyed via the ground motions can be interpreted from the measured voltages.

Fig. 1 shows the five concepts from the source to the receiver that are used in our analysis: (*1*) active source, (*2*) Green's function, (*3*) theoretical displacement, (*4*) voltage

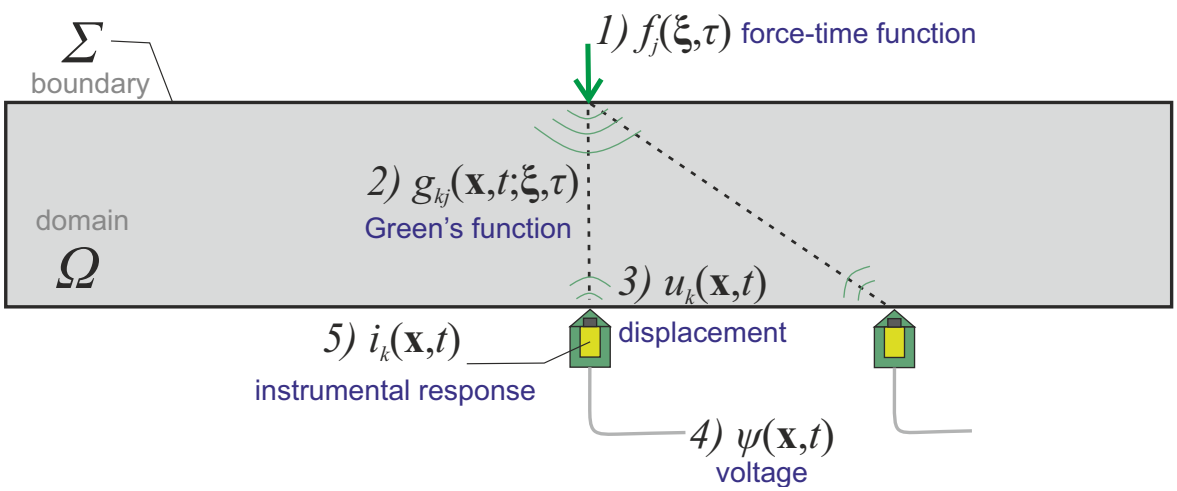

Figure 1. Schematic drawing of concepts to illustrate the operation principle of PZT sensor that link the active source to generated voltage signals measured using a data acquisition system.

signal and (*5*) instrumental response. Elastic waves propagate through a body excited by an active source. This causes vibrations through the body and theoretical displacement within or along the boundary (Σ) of the body (Ω) is estimated using Green's functions between the location of the source and receivers. The time-varying displacement along the boundary (Σ) deforms the PZT sensors and is then distorted into the voltage signal that is acquired by the data acquisition (DAQ) system. We aim to quantify the instrumental response of the PZT sensors, which is defined as the absolute calibration or characterization of PZT sensors.

Green's functions, used to map theoretical displacement to active source, are vitally important for PZT sensor characterization. McLaskey & Glaser (2012) investigated elastic stress wave propagation within a semi-infinite homogeneous and isotropic elastic plate, which was first solved by Lamb (1904) and known as "Lamb's problem". More specifically, Lamb's problem focuses on calculating the elastic disturbance caused by stress waves due to a point force in/on a half space. To find the solution of Lamb's problem (or "Green's function"), researchers numerically solved Lamb's problem starting from generalized ray theory (Johnson 1974; Pao & Gajewski 1977; Hsu 1985; McLaskey & Glaser 2012).

Two main concerns limit the application of the generalized ray theory to solve Green's

functions. First, recent advances in both laboratory-generated and *in situ* AE monitoring have shown that the corner frequency of amplitude spectra of AE events could be as low as to 1 kHz (Wu & McLaskey 2019; Villiger et al. 2020). To model this we require the spectra of Green's functions down to 1 kHz in order to calibrate PZT sensors to the same frequency band. This requires large computational loads to obtain the huge number of possible ray paths of Green's functions. Second, sample finiteness makes the semi-infinite conditions associated with Lamb's problem unrealistic for laboratory investigations and, therefore, the ray paths of side reflections from a finite elastic plate are non-negligable.

The finite element method (FEM) is an alternative and promising approach to obtain the numerical Green's function (NGF) where more realistic physical boundary conditions, similar to that of an experimental configuration, can be modelled. Although significant contributions have been made on FEM applications at the engineering-scale (e.g. tens of meters to hundreds of kilometers) with regard to elastodynamic wave propagation (e.g., Ye et al. 2016), few researchers have extended the well-developed FEM codes to calculate Green's functions between sources and receivers in laboratory experiments of PZT sensor characterization. Wu & McLaskey (2018) described a FEM analysis to obtain empirical Green's function (EGF) down to 1 kHz by modelling long-duration elastic stress wave propagation created by ball impacts of various sizes on the top surface of a thick aluminum plate. Their approach, however, requires knowledge of two separate numerical tools to obtain the EGFs. This is undoubtedly challenging since codes vary in their complexity. Moreover, previous methods employ a plate that is 'free-floating' in the air and therefore a free stress condition is applied to all boundaries.

1.3 Overview of main scientific contributions in this study

An improved description of the FEM modelling methodology to obtain NGFs from 1 kHz to 1 MHz is provided. The methodology is first validated against another approach based on the generalized ray theory (Hsu 1985) over a high-frequency range (from 100 kHz to 1 MHz) and then extended to the low-frequency analysis (from 1 kHz to 100 kHz). We investigate a variety of boundary conditions to simulate elastic stress wave propagation, reflection and transmission in/on an elastic medium excited by a unit step force-time function, and use the commercial FEM software, COMSOL Multiphysics (COMSOL AB 2019). The NGFs of a group of source-receiver pairs are obtained and then the corresponding displacement at the location of the receivers is derived.

We built a simple calibration station to perform ball impact tests over a range of diameters and used PZT sensors to measure the seismic displacement field in terms of voltage signal. Our analysis characterizes the broadband instrumental responses through accurately cropping and linking a group of segmented instrument responses over a valid frequency band in line with the solution accuracy of modelling methodology and quality of experimental data. Previous methods used to calibrate sensors have not provided the details to the multi-diameter ball drop approach – a single ball drop is simply not capable of characterizing a broadband understanding of the instrument response. As a result, observed seismic events are interpreted improperly when coverting voltages to infered seismic source properties. Moreover, we extend the instrumental response analysis from a single sensor to an array of PZT sensors from 1 kHz to 1 MHz, which is necessary to better constrain modelling efforts at the laboratory and underground laboratory scales.

2 THEORETICAL BACKGROUND AND EXPERIMENTAL SETUP

2.1 Instrumental response of PZT sensor

In Fig. 1, we study the theoretical displacement $u_k(\mathbf{x}, t)$ in the k direction throughout the medium at any location $\mathbf{x}$ and time t caused by a force-time function $f_j(\boldsymbol{\xi}, \tau)$ in the k direction at point $\boldsymbol{\xi}$ and delayed time τ. Since elastic wave propagation has linear time-invariant characteristics and due to the spatial reciprocity of the representation theorem (Aki & Richards 2002), $u_k(\mathbf{x}, t)$ can be expressed as the convolution of Green's function $g_{kj}(\mathbf{x}, t; \boldsymbol{\xi}, \tau)$ and $f_j(\boldsymbol{\xi}, \tau)$

$$u_k(\mathbf{x}, t) = g_{kj}(\mathbf{x}, t; \boldsymbol{\xi}, \tau) * f_j(\boldsymbol{\xi}, \tau), \tag{1}$$

where * denotes the convolution operation. Note that the assumption of point representation at the contact region of both the active source and PZT sensor is used, which is not exactly true due to finite area of the active source and the aperture area of the PZT sensors. This effect can be minimized by using a ball impact source and a conical-frustum PZT crystal with minimal contact area; this is discussed further in Section 2.2.

The time-varying displacement $u_k(\mathbf{x}, t)$ measured by the PZT sensors is then converted into a voltage signal $\psi(\mathbf{x}, t)$, which is recorded by a connected DAQ system. The instrumental response, $i_k(t)$, maps the measured voltage $\psi(\mathbf{x}, t)$ to the true mechanical input u_k vibration in the k direction. The mapping is assumed to satisfy a linear time-invariant system such that

$$\psi(\mathbf{x}, t) = u_k(\mathbf{x}, t) * i_k(t). \tag{2}$$

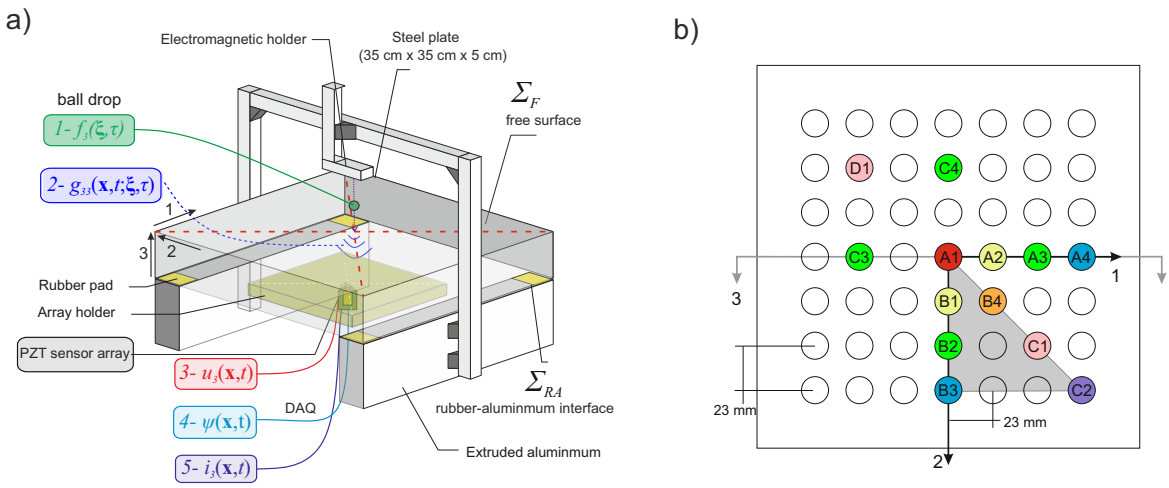

Figure 2. (a) General schematic of calibration station in the *1-2-3* directions, which consists of electromagnetic holder, steel balls with different diameters, steel transfer plate, PZT sensor array, extruded aluminum framework, etc. Concepts that link the active source to generated voltage signals are listed here: force-time function $f_3(\boldsymbol{\xi},\tau)$, Green's function $g_{33}(\mathbf{x},t;\boldsymbol{\xi},\tau)$, caused theoretical displacement $u_3(\mathbf{x},t)$, voltage signal $\psi(\mathbf{x},t)$ and instrumental response $i_3(\mathbf{x},t)$. (b) An array of PZT sensors, fixed by array holder (yellow plate in (a)). Colors indicate their epicentral locations with respect to the source.

We perform the deconvolution operation to Eq. (2) in the frequency domain to compute $I_k(\omega)$ as

$$I_k(\omega) = \frac{\Psi(\mathbf{x},\omega)}{U_k(\mathbf{x},\omega)}, \tag{3}$$

where ω denotes the ordinary frequency. $I_k(\omega)$, $\Psi(\mathbf{x},\omega)$, and $U_k(\omega)$ are variables in the frequency domain corresponding to $i_k(t)$, $\psi(\mathbf{x},t)$, and $u_k(\mathbf{x},t)$, respectively.

To obtain an accurate instrumental response $I_k(\omega)$, we present the detailed analysis of acquiring voltage $\Psi(\mathbf{x},\omega)$ in laboratory experiments (see Section 2.2) and numerically calculating Green's function $g_{kj}(\mathbf{x},t;\boldsymbol{\xi},\tau)$ (see Section 2.3). The force-time function is determined from Hertzian impact theory (Reed 1985) (see Appendix A).

2.2 Experimental setup: PZT sensor calibration station

In this section, we introduce the laboratory experiments performed on a sensor calibration station (see Fig. 2(a)). We characterize the performance of PZT sensors to measured

kinematic motion excited by elastic stress wave propagation through an elastic isotropic, homogeneous steel transfer plate due to the active source produced by a steel ball impact. A detailed comparison of characteristics, (dis)advantages and trade offs of laboratory active sources was explained by Breckenridge et al. (1990).

An extruded aluminum framework is used to support an overlaid square steel transfer plate (35 cm $\times$ 35 cm $\times$ 5 cm). Pads made of neoprene (4 yellow patches, 3 cm $\times$ 3 cm $\times$ 0.5 cm), with low mechanical impedance ($\sim$ 1/14 of steel), are used to effectively block elastic wave refraction into the aluminum framework. An electromagnetic holder is built in the upper crossbeam of the aluminum framework. Once the power is turned off, the steel ball (green) is released and drops down freely until impact at the central location of the top surface of the steel transfer plate.

In Fig. 2(b), we show 13 PZT sensors with the same KRN Services (model KRNBB-PC) mounted at the bottom surface of the steel transfer plate fixed by an array holder (see yellow plate in Fig. 2(a)). The array holder has 7 $\times$ 7 locations with 23 mm spacing in both the *1* and *2* directions, respectively. Since stress waves caused by ball impact in the *3*-direction are symmetric about the *1-3* and *2-3* planes, we have focused most of our PZT sensor converge to one quadrant of the array holder. Similar colors for the PZT sensors locations (A1 to D1) in Fig. 2(b) represent the redundant epicentral locations with respect to the source. We use the take-off angle θ to characterize 7 possible seismic ray paths between the source and PZT sensors, $\theta = 0^\circ$ (A1); 24.7° (A2, B1); 33.0° (B4); 42.6° (A3, B2, C3, C4); 52.4° (C1, D1); 54.0° (A3, B4); 62.9° (C2). The sensor performance analysis over these take-off angles is discussed in Section 5.3.

Note that the contact area between the circular tip of the KRNBB-PC sensors and the lower surface of the steel transfer plate has a radius of 0.75 mm, which is small relative to the dimension of the steel transfer plate. Also, the contact area between the ball and the

upper surface of the steel transfer plate at the time of impact is negligible. Thus we assume that the point characteristics of the source and receiver in Section 2.1 is satisfied. These sensors are sensitive to ground motion in the *3*-direction over a wide frequency range (1 kHz to 1 MHz) and their spectral characteristics have been well documented (Glaser et al. 1998; McLaskey & Glaser 2010, 2012; Selvadurai 2019; Ono 2019).

To acquire voltage $\psi(\mathbf{x}, t)$, a DAQ system (Elsys Instruments TraNET, 32 Channel TPCE-2016-4/8) is connected with the PZT sensors with a sampling frequency F_s of 20 MHz per channel. The Nyquist frequency is 10 MHz so that the F_s is adequate enough to perform sampling. Elsys AE amplifiers (AE-Amp) were used to provide the internal amplification (JFET, see Glaser et al. 1998) to sensors with 25 mA excitation and the gain was 0 dB. The detection threshold is set to 1.5 to 2 times higher than the background noise. This ensures that no acoustic signal is missed due to low signal to noise ratio (SNR), especially in the case of the impacts from the smallest steel ball.

To obtain instrumental responses, we need to perform Fast Fourier Transform (FFT) of the measured signals (Bracewell 1986) over the frequency band from $1/T_w$ to $F_s/2$, where T_w is the time window and F_s is the sampling frequency. In this case, when the frequency approaches the lower bound $1/T_w$, low resolution of amplitude spectra can occur if not enough low-frequency cycles are analyzed. A proper time window T_w is critical to accommodate trade offs between spectra resolution and computational costs in modelling the elastic wave propagation. We suggest that there should be at least $n = 8$ bins from the lowest frequency limit ($f_{min} = 1$ kHz) to its adjacent frequency 2 kHz. Since the linearly spaced increment of frequency bins $\mathrm{d}f$ equals $1/T_w$, inequations can be given as

$$\frac{f_{\min} + n\frac{1}{T_w}}{f_{\min}} \leq 2, \tag{4}$$

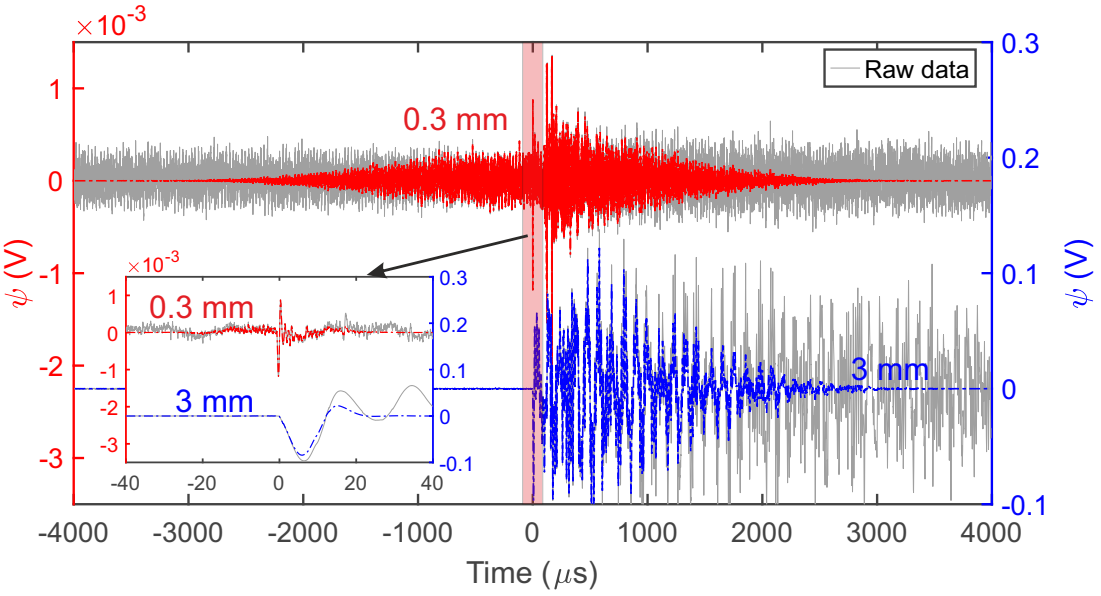

Figure 3. Raw data (gray) and windowed data (colored) centered at the first P-wave arrival from typical acoustic events due to ball impact, with diameters of 0.3 (red) and 3 mm (blue), measured by the PZT sensor A1 located directly beneath the impact point. Window functions with two lengths 80 μs (see inset) and 8000 μs are used for high- and low-frequency analysis in Section 4, respectively.

$$T_w \geq \frac{n}{f_{\min}}, \tag{5}$$

where a window length of $T_w = 8000$ μs is used to crop caused voltage $\psi(\mathbf{x}, t)$ and displacements $u_3(\mathbf{x}, t)$ with an identical length.

To avoid spectral leakage, a symmetric window function with the same length as $\psi(\mathbf{x}, t)$ and $u_3(\mathbf{x}, t)$ is essential. In Fig. 3, we show the raw data (gray line) of $\psi(\mathbf{x}, t)$ for typical acoustic events due to ball impacts with diameters of 0.3 and 3 mm. A 8000-μs Blackman–Harris window function $win(t)$ (centered about the first P-wave arrival) is used throughout this study to obtain windowed signals (red and blue lines). The windowed signals have the maximum in the middle, and taper away from the middle. By performing FFT to the windowed $\psi(\mathbf{x}, t)$ and $u_3(\mathbf{x}, t)$, and neglecting the phase information, we obtain

$$|U_3(\mathbf{x}, \omega)| = |\mathcal{F}\{g_{33}(\mathbf{x}, t; \boldsymbol{\xi}, \tau) * f_3(\boldsymbol{\xi}, \tau) \cdot win(t)\}|, \tag{6}$$

Table 1. Material parameters of the steel ball, steel transfer plate and neoprene pad used in the calibration station.

Parameter	Symbol	Value		
		steel ball	steel transfer plate	neoprene pad
Type		GCr15	HABA CK45	NBR L8000
Young's modulus (GPa)	E	210	210	
Possion's ratio	ν	0.303	0.27	
Density (kg/m^3)	ρ	7800	7850	1490
P wave velocity (m/s)	c_p		5782	2690
S wave velocity (m/s)	c_s		3245	1340
Dimension (mm)		[0.3, 0.35, 0.4, 0.5, 0.6, 0.7, 0.8, 1.0, 1.5, 2.0, 2.5, 3.0]	350 × 350 × 50	30 × 30 × 5

$$|\Psi(\mathbf{x},\omega)| = |\mathcal{F}\{\psi(\mathbf{x},t)\cdot win(t)\}|, \tag{7}$$

where $|U_3(\mathbf{x},\omega)|$ and $|\Psi(\mathbf{x},\omega)|$ are the amplitude spectra of windowed $\psi(\mathbf{x},t)$ and $u_3(\mathbf{x},t)$, respectively. $|\cdots|$ represents the absolute value operator. $g_{33}(\mathbf{x},t;\boldsymbol{\xi},\tau)$ is the 33-component of Green's function that maps the measured displacement $u_3(\mathbf{x},t)$ in the 3-direction to the ball drop impact force $f_3(\mathbf{x},t)$ in the 3-direction. The details of Green's function are discussed further in Section 2.3.

Finally, Eq. (3) can be written as

$$I_3(\omega) = \frac{|\Psi(\mathbf{x},\omega)|}{|U_3(\mathbf{x},\omega)|} = \frac{|\mathcal{F}\{\psi(\mathbf{x},t)\cdot win(t)\}|}{|\mathcal{F}\{g_{33}(\mathbf{x},t;\boldsymbol{\xi},\tau) * f_3(\boldsymbol{\xi},\tau)\cdot win(t)\}|}, \tag{8}$$

where $\cdot$ denotes dot product, and $\mathcal{F}\{\}$ represents the FFT operation.

Material parameters of the steel ball, steel transfer plate and neoprene pad used in the calibration station are summarized in Table 1.

2.3 Green's function

We now aim to obtain Green's function, $g_{33}(\mathbf{x},t;\boldsymbol{\xi},\tau)$, which reflects the displacement component in the 3-direction due to time-delayed Dirac delta (true impulse), $\delta(t-\tau)$ in the 3-direction. However, it is not easy to implement $\delta(t-\tau)$ numerically. Instead, we use the

Heaviside step function, $H(t-\tau)$, which is the integral of $\delta(t-\tau)$ with respect to time. The corresponding $f_3(\boldsymbol{\xi},\tau)$ can be expressed as

$$f_3(\boldsymbol{\xi},\tau) = \delta(\mathbf{x}-\boldsymbol{\xi})H(t-\tau), \tag{9}$$

where $\delta(\boldsymbol{x}-\boldsymbol{\xi})$ denotes the spatial source distribution of the Dirac delta function. In this study, $\delta(\boldsymbol{x}-\boldsymbol{\xi})$ is described as a limit representation of the Dirac delta

$$\delta(\mathbf{x}-\boldsymbol{\xi}) = \lim_{S\to 0}\frac{1}{\sqrt{\pi S}}e^{-\frac{(\mathbf{x}-\boldsymbol{\xi})^2}{S}}, \tag{10}$$

where S is associated with the mesh size in the vicinity of the ideal loading point; its exact value is discussed in Section 3.2. The $u_3(\mathbf{x},t)$ due to $f_3(\boldsymbol{\xi},\tau)$ is given by

$$\begin{aligned} u_3(\mathbf{x},t) = g_{33}(\mathbf{x},t;\boldsymbol{\xi},\tau) * f_3(\boldsymbol{\xi},\tau) &= g_{33}(\mathbf{x}-\boldsymbol{\xi},t-\tau) * \{\delta(\mathbf{x}-\boldsymbol{\xi})H(t-\tau)\} \\ &= \{g_{33}(\mathbf{x}-\boldsymbol{\xi},t-\tau) * \delta(\mathbf{x}-\boldsymbol{\xi})\} * H(t-\tau) \\ &= g_{33}(\mathbf{x},t-\tau) * H(t-\tau). \end{aligned} \tag{11}$$

Recalling the linear time-invariant characteristics of convolution in Section 2.1 and the properties of convolution differentiation (Bracewell 1986), we can conduct time differentiation operation on Eq. (11)

$$\begin{aligned} v_3(\mathbf{x},t) = \frac{\partial u_3(\mathbf{x},t)}{\partial t} &= g_{33}(\mathbf{x},t-\tau) * \frac{\partial H(t-\tau)}{\partial t} \\ &= g_{33}(\mathbf{x},t-\tau) * \delta(t-\tau) \\ &= g_{33}(\mathbf{x},t). \end{aligned} \tag{12}$$

Therefore, Green's function $g_{33}(\mathbf{x},t)$ is derived as the particle motion velocity in the *3*-

direction, $v_3(\mathbf{x}, t)$, caused by the force-time function $H(t-\tau)$ with a spatial distribution described by Eq. (10).

3 MODELLING

In this section, we present the FEM-based methodology (i.e., governing equations, modelling parameters) to calculate NGFs. We validate the methodology against the reference approach over a high-frequency band (from 100 kHz to 1 MHz) and then extend it to low-frequency analysis down to 1 kHz.

3.1 Governing equations

We simulate the elastic wave propagation using the state-of-art discontinuous Galerkin (DG) FEM by COMSOL Multiphysics (COMSOL AB 2019). The steel transfer plate and neoprene pads are modelled explicitly and their material properties are provided in Table 1. The particle motion velocity, $\boldsymbol{v}$, and strain, $\boldsymbol{E}$, with the implementation for steel ($k=1$) and neoprene ($k=2$) domains, obey the first-order elastodynamic equations

$$\rho^k \frac{\partial \boldsymbol{v}}{\partial t} - \nabla \cdot \boldsymbol{S} = \boldsymbol{f}, \tag{13a}$$

$$\frac{\partial \boldsymbol{E}}{\partial t} - \frac{1}{2}\left[\nabla \boldsymbol{v} + (\nabla \boldsymbol{v})^{\boldsymbol{T}}\right] = \boldsymbol{0}, \tag{13b}$$

$$\boldsymbol{S} = \boldsymbol{C}^k : \boldsymbol{E}, \tag{13c}$$

where ρ^k stands for the material density, $\boldsymbol{S}$ denotes the Cauchy stress tensor, and $\boldsymbol{f}$ is the applied loading described by Eq. (9). $\boldsymbol{C}^k$ represents the isotropic stiffness tensor characterized by Young's modulus, E, and Poisson's ratio, ν. To guarantee the uniqueness of $\boldsymbol{v}$ and

$\boldsymbol{E}$, the zero-traction condition is enforced on the free surface Σ_{F} of the steel transfer plate (see Fig. 2(a)), that is

$$\boldsymbol{n} \cdot \boldsymbol{S} = \boldsymbol{0}, \tag{14}$$

where $\boldsymbol{n}$ is unit normal vector. By incorporating numerical flux, DG FEM weakly imposes mechanical continuity of $\boldsymbol{v}$ and $\boldsymbol{E}$ across the interior boundary, which is especially computationally efficient for studying 3D transient wave problems (Ye et al. 2016).

To model elastic stress wave transmission and reflection along the interface, Σ_{RA} (see Fig. 2(a)) between the neoprene pads and aluminum framework, we impose a velocity-dependent traction on Σ_{RA}. This traction is caused by the non-zero mechanical impedance of the aluminum framework ($k = 3$) and can be written as a combined effect of P- and S-waves (Cohen & Jennings 1983)

$$\boldsymbol{n} \cdot \boldsymbol{S} = -\rho^k c_p^k \left(\boldsymbol{v} \cdot \boldsymbol{n}\right) \boldsymbol{n} - \rho^k c_s^k \left(\boldsymbol{v} \cdot \boldsymbol{t}\right) \boldsymbol{t}, \tag{15}$$

where ρ^k, c_p^k, c_s^k are the P- and S- wave velocity of aluminum, respectively, and $\boldsymbol{t}$ is the unit tangent vector.

3.2 Modelling parameters

In this section, we describe how the numerical calculations are performed to obtain NGFs, including the meshing schemes, time step and simulation procedures.

For meshing schemes, one of most critical issues is to choose an optimized mesh size; a relatively coarse grid works in a similar manner to a high-pass filter (HPF), leading to inaccurate NGF solutions whereas a very fine grid results in huge computational consumption (in terms of memory and CPU time). To produce a satisfactory solution, the maximum size

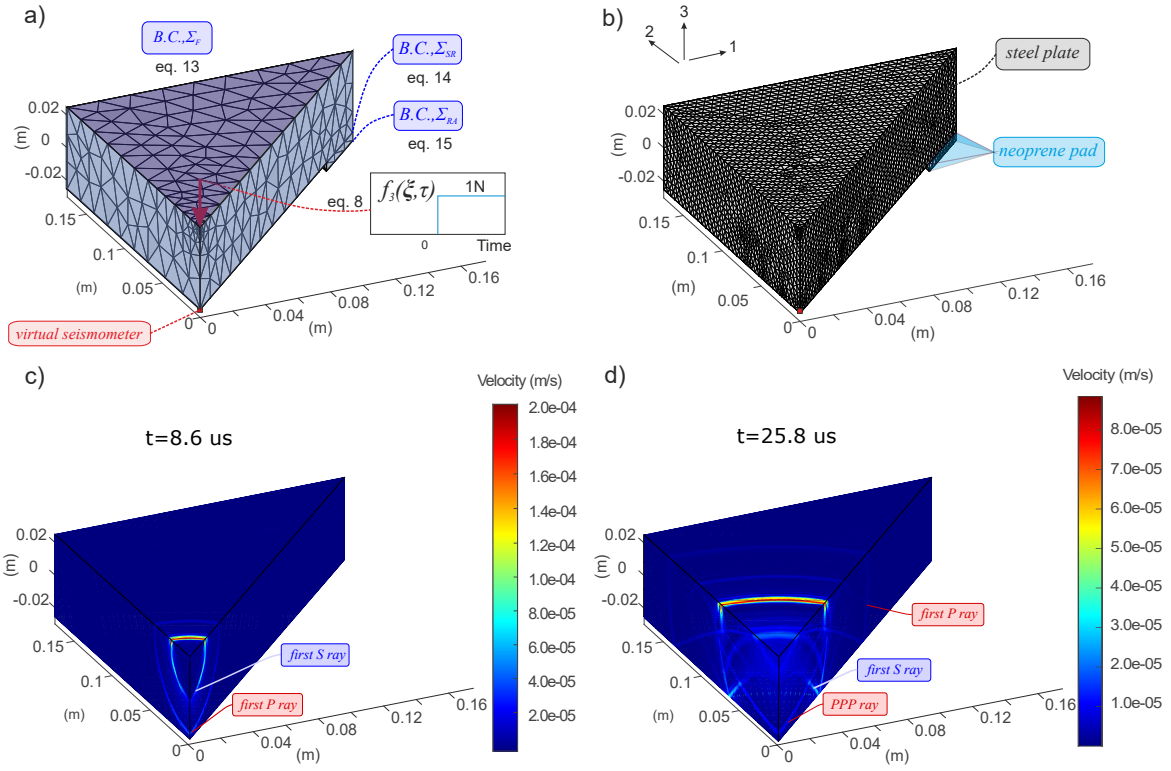

Figure 4. 1/8 symmetric modelling configuration visualized in the *1-2-3* directions to study laboratory elastic wave propagation caused by unit step force-time function. Boundary conditions are schematically shown to constrain the wave propagation problem. (a) *c-FEM* model with a coarse grid, (b) *f-FEM* model with a fine grid. The magnitude of the particle motion velocity field, acquired from the results of the *f-FEM* model, are visualized at time 8.6 μs (c) and 25.8 μs (d), respectively. Note that the time $t = 0$ is when the unit step force-time function is applied.

h of the mesh elements should be lower than the wavelength of interest λ (typically a ratio lower than 1). Since higher-order Lagrange interpolation functions, up to the forth order, are utilized, this ratio could be set as a larger value (COMSOL AB 2019). In this study, the ratio is assumed to be 1, that is $\frac{h}{\lambda} = 1$, where $\lambda = \frac{c_p}{\omega_0}$, λ, c_p denote the wavelength and velocity of P-wave, and ω_0 represents the upper limit of the bandwidth of interest. Even when using the efficient DG FEM, it is still time-consuming to calculate high-frequency NGFs. To reduce the computational cost, the adaptive grid scheme in FEM, can be adopted; however, this, is a non-trivial task. To remedy this, we introduce two separate simulations, which include a low-frequency model with a relatively coarse grid (*c-FEM*), and a high-frequency model with a relatively fine grid (*f-FEM*).

Due to the geometric symmetry of the calibration station, only $\frac{1}{8}$ of the steel transfer

plate and neoprene pad was modelled. We set ω_0^c = 300 kHz (>100 kHz) and ω_0^f = 1.2 MHz (>1 MHz) to control h, where the superscripts c and f stand for *c-FEM* and *f-FEM*, respectively. The mesh around the center of loading area (red arrow) was locally refined to ensure a correctly applied $f_3(\boldsymbol{\xi}, \tau)$. We determine the S value from Eq. (10) as 1e-6 (units: $1/m^2$) by comparing the numerical integration of normal stress around the loading against $f_3(\boldsymbol{\xi}, \tau)$. The Delaunay tessellation method is adopted to create a tetrahedral mesh. Grid discretizations of models simulated in *c-FEM* and *f-FEM* are shown in Fig. 4(a) and (b), which have 762 and 104624 unstructured tetrahedral quartic elements, respectively. Details of material properties and the geometry information are given in Table 1.

The Courant–Friedrichs–Lewy (CFL) condition is adopted to determine the stable time step, Δt, which is automatically optimized by COMSOL Multiphysics. During our simulations, the 4^{th} explicit Runge-Kutta (RK) method is adopted. Note that we use a pseudo-step loading scheme in the modellings. In this case, when we enforce a unit step force-time function to the loading point, there is a small 'rise time', τ_r, to reach the peak loading. By probing the real applied force history around the loading point (see arrow in Fig. 4), we found that τ_r is between 5 and 10 nanoseconds for *c-FEM* and *f-FEM*. Considering the fact that the force-time function of glass capillaries fracturing has a τ_r of approximately 200 nanoseconds while most of its spectral energy does not fall below 2 MHz (Selvadurai 2019), this pseudo-step loading scheme has little effect on the spectrum over the bandwidth of interest.

For modelling procedures, we simulate *c-FEM* for 4000 μs and *f-FEM* for 40 μs (half length of suggested time window in Eq. (5)) such that the spectra resolution is satisfied down to 1 kHz and 100 kHz, respectively. We obtain time-varying $v_3(\mathbf{x}, t)$ probed at the location

of the virtual seismometer (red square in Fig. 4(a)) and derive the NGFs from both models by means of the transformation described by Eq. (12).

3.3 Model validation: high-frequency analysis of elastic waves

In above section, we propose using ω_0^c and ω_0^f to control the mesh size such that the frequency component of NGF can be expected to be kept below 100 kHz and 1 MHz. Our aim is to validate the capabilities of these models and find the corresponding valid frequency band beyond which the calculated NGFs deviate from reference results. Note that the reference ("true") results are computed by an approach based on the generalized ray theory (*GR*) (Hsu 1985; McLaskey & Glaser 2012) that governs transient wave propagation in a semi-infinite purely elastic plate.

Fig. 4(c) and (d) show the magnitude of the particle motion velocity (units: m/s) to qualitatively illustrate the performance of the *f-FEM* model in simulating elastic wave propagation. We see that the elastic wave initiates from the loading point and geometrically spreads. Fig. 4(c) shows the first P-wave ray around the virtual seismometer and the first S-wave ray that follows at time 8.6 μs. The spatial distance between the wavefront of the first P- and S-wave is controlled by the wave propagation times and the speed difference between them.

In Fig. 4(d), we observe multiple reflections of different rays of the propagated elastic waves between the upper and lower surface of the steel plate at time 25.8 μs: first P-wave, first S-wave, PPP-wave, etc. The PPP-wave ray is shown around the virtual seismometer. These rays are important since they offer important information and frequency content in the velocity seismogram. We note that here we are only showing validation efforts for scenarios where the virtual seismometer is located directly below the source; however, this methodology can be extended to more source-receiver pairs (see Section 5.3), which will be a major benefit once the validation is complete.

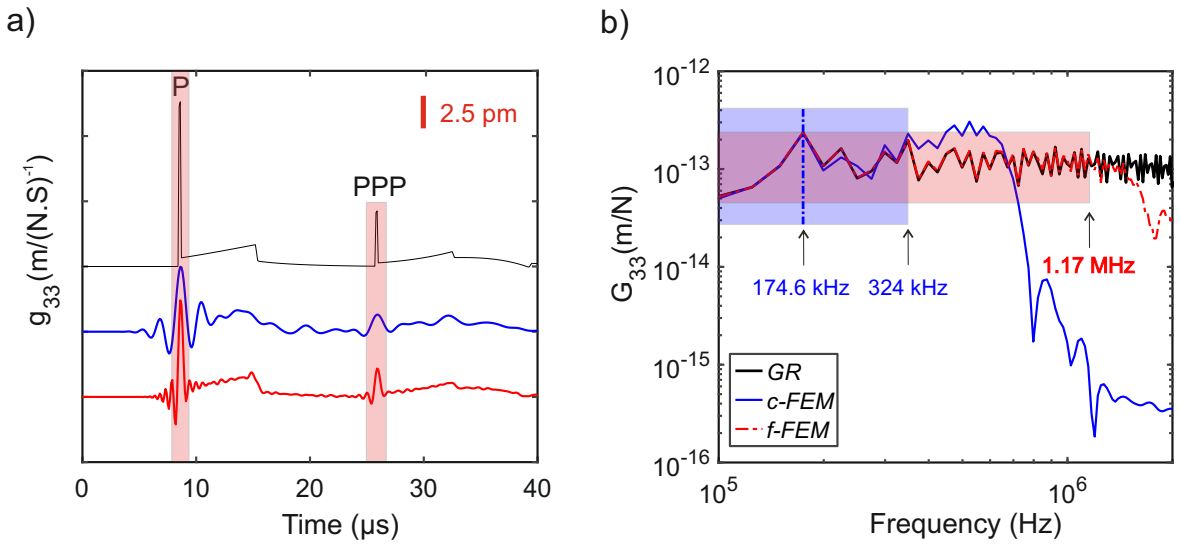

Figure 5. Comparison of Green's function from *GR* (black line), *c-FEM* (blue line) and *f-FEM* (red line), in (a), time domain (offset vertically for better comparison), and (b), frequency domain. In (a), first P and reflected PPP phase of the elastic waves was captured and windowed inside the 2 pink bars, respectively. In (b), the blue and pink patches mark the valid bandwidth where the modelling results match well with that of the generalized ray theory.

We now validate the NGFs evaluated at the virtual seismometer over a short duration. The seismometer starts calculating $v_3(\mathbf{x}, t)$ from the instantaneous loading until the initial side reflection back. In our case, this duration is not allowed to exceed 60 μs so that NGF should, theoretically, be the same as that of the semi-infinite elastic plate since the wavefront has not reached the edges of the transfer plate. We simulated both *c-FEM* and *f-FEM* and the *GR* for 40 μs under the loading described by Eq. (9).

Fig. 5(a) presents solutions of the time-domain Green's function calculated by a reference approach *GR* (black line), *c-FEM* (blue line) and *f-FEM* (red line), respectively. Green's function from *GR* shows sharp peaks for the P and PPP phases of the elastic waves, which reflect the singularities of 'true' Green's functions at either P or PPP arrivals (Johnson 1974). The NGF from *f-FEM* can also capture similar behavior as the *GR* but has more oscillation near the sharp peaks associated with the phase arrivals. This oscillation is mainly due to the Gibbs phenomena (Bracewell 1986), as the piece-wise high-order Legendre basis function is used in FEM modelling.

Fig. 5(b) shows the amplitude spectra of NGFs in the frequency domain. The amplitude spectrum calculated using the *GR* approach is almost flat below 2 MHz the *GR* solution is semi-analytical. For NGFs from FEM modelling, the amplitude spectra match well with these of the *GR* when the frequency ranges from 100 to 324 kHz (for *c-FEM*) and from 100 to 1.17 MHz (for *f-FEM*). However, the NGFs from both the *c-FEM* and *f-FEM* deviate rapidly from that of the *GR* around 324 kHz and 1.17 MHz, which corresponds approximately to the proposed ω_0^c and ω_0^f. The capabilities of both the *c-FEM* and *f-FEM* simulations are validated: we obtain accurate NGFs up to 100 kHz from the *c-FEM* and to 1 MHz from *f-FEM*. Note that to increase the accuracy, we consider that the NGF from the *c-FEM* model is valid up to 174.6 kHz instead of 324 kHz. After validating the capabilities of our built model with a simple geometry boundary, now we have a tool for studying elastic wave propagation that can accommodate realistic geometries with a validated level of accuracy.

3.4 Model extension: low-frequency analysis of long-duration excitation down to 1 kHz

We extend the capability of *c-FEM* to perform low-frequency analysis by elongating the simulation duration. Due to the finite dimension of the calibration station, the simpler Lamb problem, where only the elastic wave reflection between the bottom and top surface of the steel transfer plate is modelled, is no longer valid. To study the effects of realistic boundaries on the elastic wave propagation problem, we conducted the following three modelling scenarios:

- *float-NF*: modelling the elastic wave propagation through an unsupported/floating steel transfer plate. We adopt similar boundary conditions (free of stress over all surfaces of the tested specimen) to those used in Wu & McLaskey (2018) and construct a *float* model.
- *float-HP*: in the *float* model, rigid body motion occurs because there are no constraints

from the supported material (i.e., the neoprene pad beneath the steel plate) are modelled. To correct the NGFs imposed by improper boundary conditions, we process the raw $v_{33}(\mathbf{x}, t)$ using a minimum-order high-pass filter. This filter has a stopband attenuation of 60 dB and a passband frequency of 1 kHz.

- *true BC*: to better model the real elastic wave propagation, more physical boundary conditions, described by Eqs. (14) and (15) were already introduced in the *c-FEM* model to simulate the elastic wave reflection and refraction occurring at the interfaces of the steel transfer plate, neoprene pads and aluminum framework.

We extract $v_{33}(\mathbf{x}, t)$ with a duration of 8000 μs (centered at the first P-wave arrival) in the above scenarios and use the transformation (see Eq. (12)) to obtain the NGFs for the same source-receiver pair. By performing FFT and neglecting the phase information, we obtain the amplitude spectra of low-frequency NGFs, which are termed as *float-NF* (blue line in Fig. 6(a)), *float-HP* (black line in Fig. 6(a)) and *true BC* (red line in Fig. 6(a)) corresponding to the three scenarios given above, respectively.

In Fig. 6(a), *float-NF* tends to decrease 'linearly' from ∼1e-12 to ∼1e-14 m/N from 1 kHz and 100 kHz. The large amplitude of low-frequency components is caused by the rigid body motion of the steel transfer plate. By performing a high-pass filter operation on *float-NF*, the rigid body motion is significantly removed. We see that the *float-HP* has a relatively flat spectrum with few distinct spectral peaks representing the low-frequency resonances and anti-resonances of mechanical vibration. The resonant frequencies from *float-HP* and *true BC* match well over 1 to 100 kHz, demonstrating that a consideration of the true physical boundaries has little effect on the shift of the resonant frequency.

For a better comparison, we plot the ratio of *true BC* to *float-HP* from 1 to 100 kHz in Fig. 6(b). From 1 to 10 kHz, the ratio at the locations of resonant and anti-resonant

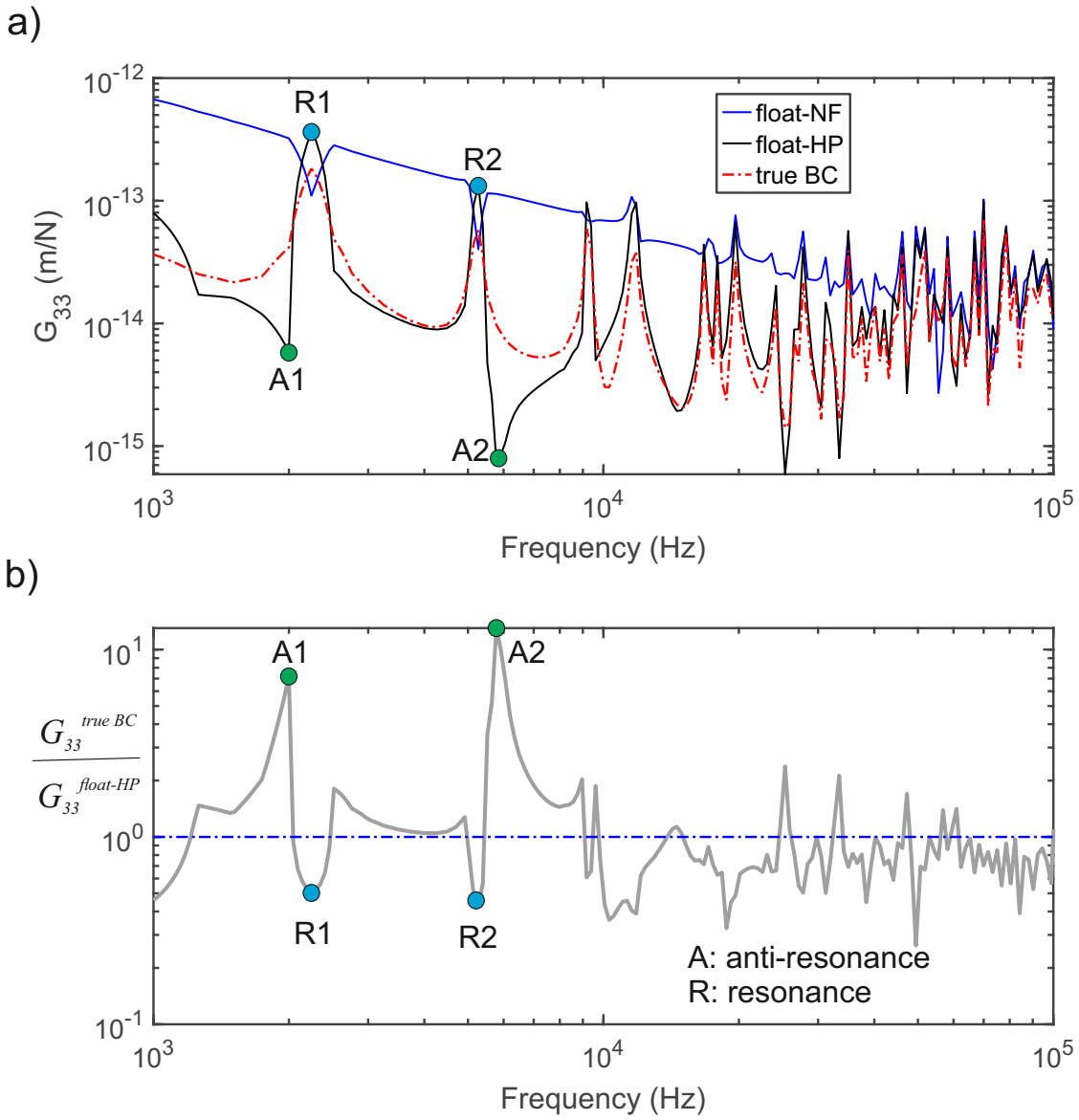

Figure 6. (a) Comparison of NGFs calculated from three modelling scenarios: *float-NF* (blue line), *float-HP* (black line) and *true BC* (red line). (b) Ratio of NGFs from *true BC* to that of *float-HP*. Locations of resonant and anti-resonant frequencies are labelled as R and A, respectively.

frequencies deviates significantly from 1. These locations are labelled A (anti-resonance) and R (resonance). We find that around the resonant frequency (i.e., *R1* and *R2*), the *true BC* is nearly half the *float-HP*. Conversely, around the anti-resonant frequency, the *true BC* can be 7 to 13 times than of the *float-HP*. This ratio tends to be flat and close to 1 for frequencies between 10 to 100 kHz. This suggests that both scenarios have similar NGFs over 10 to 100 kHz.

We modelled how the physical constraints resulting from the experimental configuration affected the elastic wave propagation problem. We interpret the results from the realistic boundary conditions. Kinematic energy of the elastic stress waves initially flows from the loading point, travels through the steel transfer plate and neoprene pads, and finally leaves the *c-FEM* model naturally where the spatiotemporal evolution of the energy field is dominated by properties of both media (steel plate, neoprene pads) and their interfaces. No extra high-pass filter operation is needed to remove the low-frequency component of the kinematic energy, which is fully trapped inside the steel transfer plate in the *float* model. Therefore, the constructed *c-FEM* model can be utilized to obtain the NGF in a more physical way, which becomes important when more complex geometries and boundary conditions are applied. To solve the multiphysics problem of elastic wave propagation, our constructed models can potentially be integrated with state-of-the-art multiphysics couplings (i.e. temperature and fluids) from the COMSOL Multiphysics software whose abilities have been validated against theoretical solutions and/or laboratory experiments in the geomechanics communities (Gasch et al. 2016; Selvadurai & Najari 2013, 2017; Selvadurai et al. 2015; Selvadurai & Selvadurai 2014; Selvadurai & Suvorov 2017).

4 PZT SENSOR CHARACTERIZATION USING THE BALL IMPACT EXPERIMENT

In the above sections, we described the FEM-based methodology used to obtain high-frequency NGFs from 100 kHz to 1 MHz as well as low-frequency counterparts from 1 to 100 kHz. We now use the source from a ball impact experiment to generate theoretical $f_3(t)$. To obtain $u_3(\mathbf{x}, t)$, we performed the convolution of NGFs with $f_3(t)$ (from 0 to t_c). For details of characterization experiments, refer to Section 2.2.

To obtain a nearly flat spectrum of $f_3(t)$ from 1 kHz to 1 MHz, we dropped a series

of steel balls with different diameters from the same height. The impact from balls with a small diameter (i.e., 0.3 mm) has a rise time ($\sim$ 0.5 μs) and imposes a high-frequency mechanical pulse resulting in spectral energy concentrated well below its corner frequency (e.g. $\geq$ 1 MHz). Conversely, the ball impact with relatively large diameter balls (e.g. 3 mm) has a much longer rise time ($\sim$ 4.7 μs) where most of the spectrum energy is concentrated under the low-frequency bandwidth (from 1 to 100 kHz).

Larger diameter (e.g. 10 mm) ball impacts were performed and we found that the response of the PZT sensor used was saturated. For this reason, smaller diameter balls were used. Schnabel et al. (2017) dropped balls of varying diameter (1.5 to 10 mm) onto a disk plate with a diameter of 103.8 mm. They found that when the contact time is extended by performing larger ball impacts, the elastic waves resulting from the impact and subsequent boundary reflections interacted with each other. As a result, the convolution between $f_3(t)$ and $g_{33}(\mathbf{x}, t)$ does not hold true and $u_3(\mathbf{x}, t)$ cannot be obtained. Therefore, we needed to evaluate the contact time t_c and ensure that the travel time of the elastic waves was (at minimum) twice the plate thickness. Sensor saturation and convolution ineffectiveness are two factors that are under reported in the literature and, considered together, constrained the largest ball diameter to 3 mm in this study.

The same drop height h_d = 138 mm was used for all impact tests; this was high enough to generate mechanical vibrations that could be measured by PZT sensors over all take-off angles. We repeated dropping the steel ball 5 times with 10 diameters (0.3, 0.35, 0.4, 0.5, 0.6, 0.7, 0.8, 1, 1.5, 2, 2.5, 3 mm). Note that the detection threshold set in the DAQ system needs to be adjusted with the various source intensities associated with the ball diameter. We introduced data processing techniques described in Section 2.2 to determine $u_3(\mathbf{x}, t)$ and $\psi(\mathbf{x}, t)$, which were used to obtain the segmented amplitude spectra of displacement $|U_3|$ and voltage $|\Psi|$, from Eqs. 6 and 7, respectively.

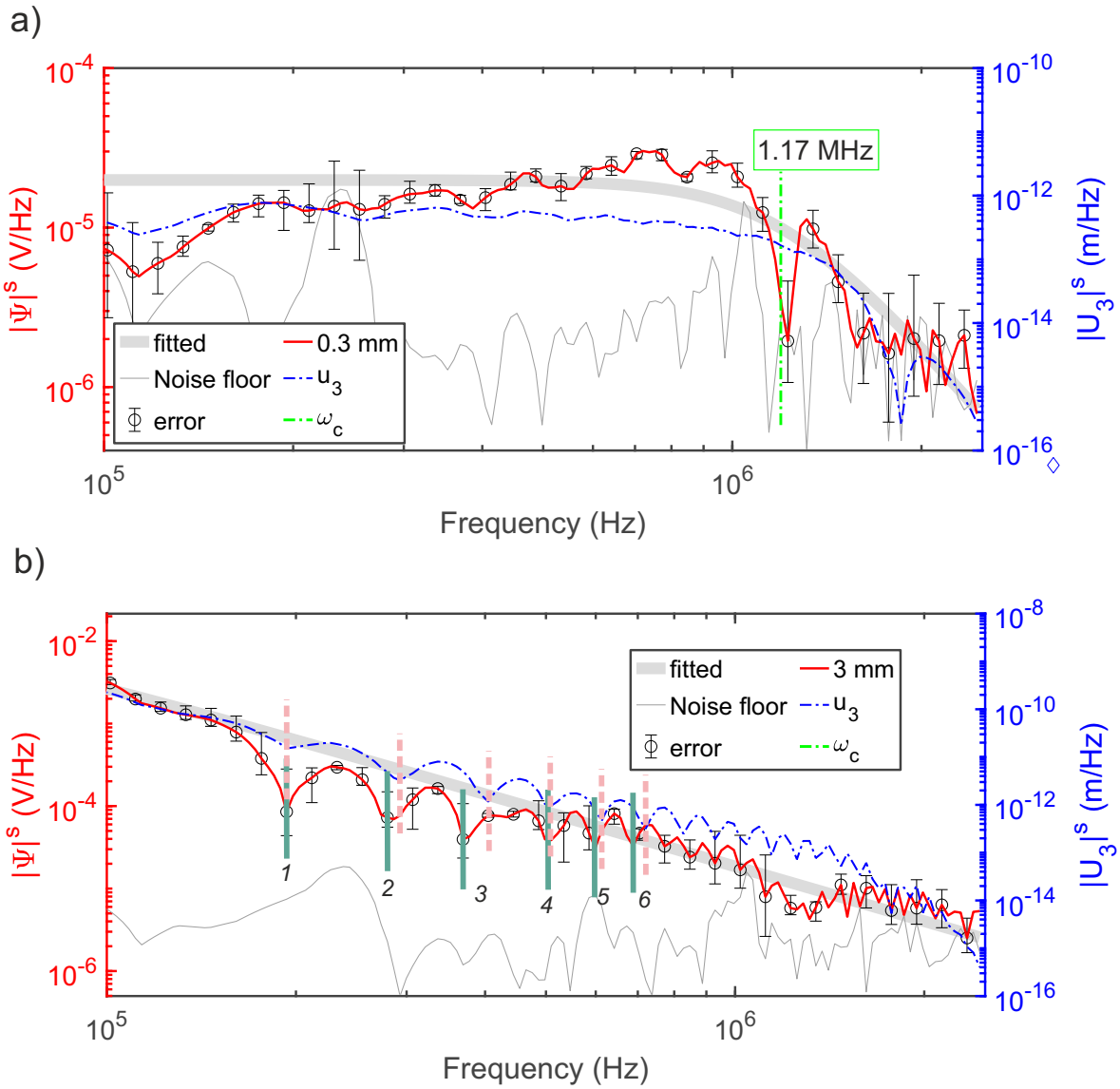

Figure 7. Amplitude spectra of voltage $|\Psi|^s$ (red line), background noise (thin gray line), *Omega-n* model (thick gray line) and displacement $|U_3|^s$ (blue line) of (a) 0.3 mm and (b) 3mm diameter ball impacts over a short duration (80 μs). In (b), a group of local minima of $|U_3|^s$ (pink dash line) and $|\Psi|^s$ (green line) are labelled to show the horizontal offset.

4.1 Short-duration excitation (100 kHz to 1 MHz)

In this section, we windowed the raw voltage caused by short-duration (80 μs, denoted by superscript s) excitation of 0.3 and 3 mm ball impacts as shown in the inset region of Fig. 3. The time $t = 0$ is when first P-wave arrives.

The amplitude spectra of $|\Psi|^s$ and $|U_3|^s$ due to the 0.3 mm ball impact from 100 kHz to 2.5 MHz are shown in Fig. 7(a). Since we are interested in the plateau part of the amplitude

spectrum, we need to determine the corresponding corner frequency ω_c. We use the *Omega-n* model, which has been shown to well-characterize both the ball impact spectra (McLaskey et al. 2015) and earthquake spectra (Hanks 1979). To obtain ω_c, we performed spectral fitting of $|\Psi|^s$:

$$\Omega(\omega) = \frac{\Omega_0}{1 + (\omega/\omega_c)^n}, \tag{16}$$

where Ω initially refers to earthquake displacement spectra but is also useful due to the similarties to the ball drop placement spectra (McLaskey et al. 2015). In this study, Ω refers to $|\Psi|^s$. Ω_0 denotes the plateau amplitude, n is the absolute value of the slope describing the high-frequency falloff. The ω_c and n to be fitted are bounded from 100 kHz to 2.5 MHz and from 1 to 5, respectively. Researchers suggest that the amplitude spectra of groud motion due to ball drop can be generally characterized by Eq. 16 (McLaskey et al. 2015; Selvadurai 2019). The ω_c is determined as 1.17 MHz (green line) in Fig. 7(a) and the fitted result is plotted as the thick gray line.

The relative error of $|\Psi|^s$ (black error bar) among the repeated tests (5 times) is shown. Minor variations suggest that the ball impact is a very repeatable mechanical source and works well at high-frequencies below ω_c. The variations in the noise floor was obtained by cropping the background noise data with same length as $|\Psi|^s$. The amplitude spectra of noise floor array was obtained through the same procedures to obtain $|\Psi|^s$. We see the SNR (signal-to-noise ratio) is continuously larger than 1 from almost 250 kHz to 1 MHz and this acts as an indicator to crop a valid frequency band of $|\Psi|^s$.

Fig. 7(b) presents the results from a 3 mm ball impact. We note that both $|U_3|^s$ (blue line) and $|\Psi|^s$ (red line) fall off rapidly with an almost constant slope (gray line) fitted from a series of "lobes" while the fitted ω_c is fixed at 100 kHz. This means that we could not

crop valid $|U_3|^s$ and $|\Psi|^s$ segmentations from 100 kHz to 1 MHz. We suggest that these lobes are caused by a group of local minima and maxima impact that forces itself in the phase of spectrum energy fall off in accordance with Eq. (A.3). By labelling the local minima (i.e., *1, 2, 3, 4, 5, 6, ...*) of $|U_3|^s$ (pink dash line) and $|\Psi|^s$ (green solid line), we find there exists a horizontal offset of frequency. The resulting analysis of ball impact tests shows that from the smallest (0.3 mm) to the largest (3 mm) size, changes in the momentum of the relatively large balls and their impact (e.g. 3 mm) can damage the steel transfer plate and cause greater associated plastic deformation of the steel transfer plate. As a result, Reed's elastic impact theory (Appendix A and Reed 1985) does not work accurately at high-frequencies for larger diameter ball drops.

4.2 Long-duration excitation (1 kHz to 100 kHz)

In this section, we extend the short-duration analysis to long-duration case (8000 μs, denoted by superscript l). The raw and windowed $\psi(\mathbf{x}, t)^l$ caused by 0.3 mm and 3 mm ball impacts are shown in Fig. 3.

Following the same data processing technique given in Section 4.1, we obtain the amplitude spectra of voltage $|\Psi|^l$ and displacement $|U_3|^l$ from 0.3 mm ball impact testing. In Fig. 8(a), both $|U_3|^l$ (blue line) and $|\Psi|^l$ (red line) are relatively flat from 1 kHz below the corner frequency ω_c (1.27 MHz, green line) of $|\Psi|^l$. The displacements $|U_3|^l$ are calculated from the *c-FEM* model, which is only validated below 174.6 kHz from the methodology validation (see Section 3.3). We see that the amplitude spectrum of the noise floor almost overlaps with or even higher than $|\Psi|^l$ below 174.6 kHz. Therefore $|\Psi|^l$ from 1 to 174.6 kHz cannot be used with $|U_3|^l$ for further analysis of I_3, see Eq. (8).

By incrementally increasing the ball diameter until 3 mm, we obtain the corresponding $|\Psi|^l$ and $|U_3|^l$ as shown in Fig. 8(b). We find ω_{min} as the minimum between $\omega_c = 71.1$ kHz

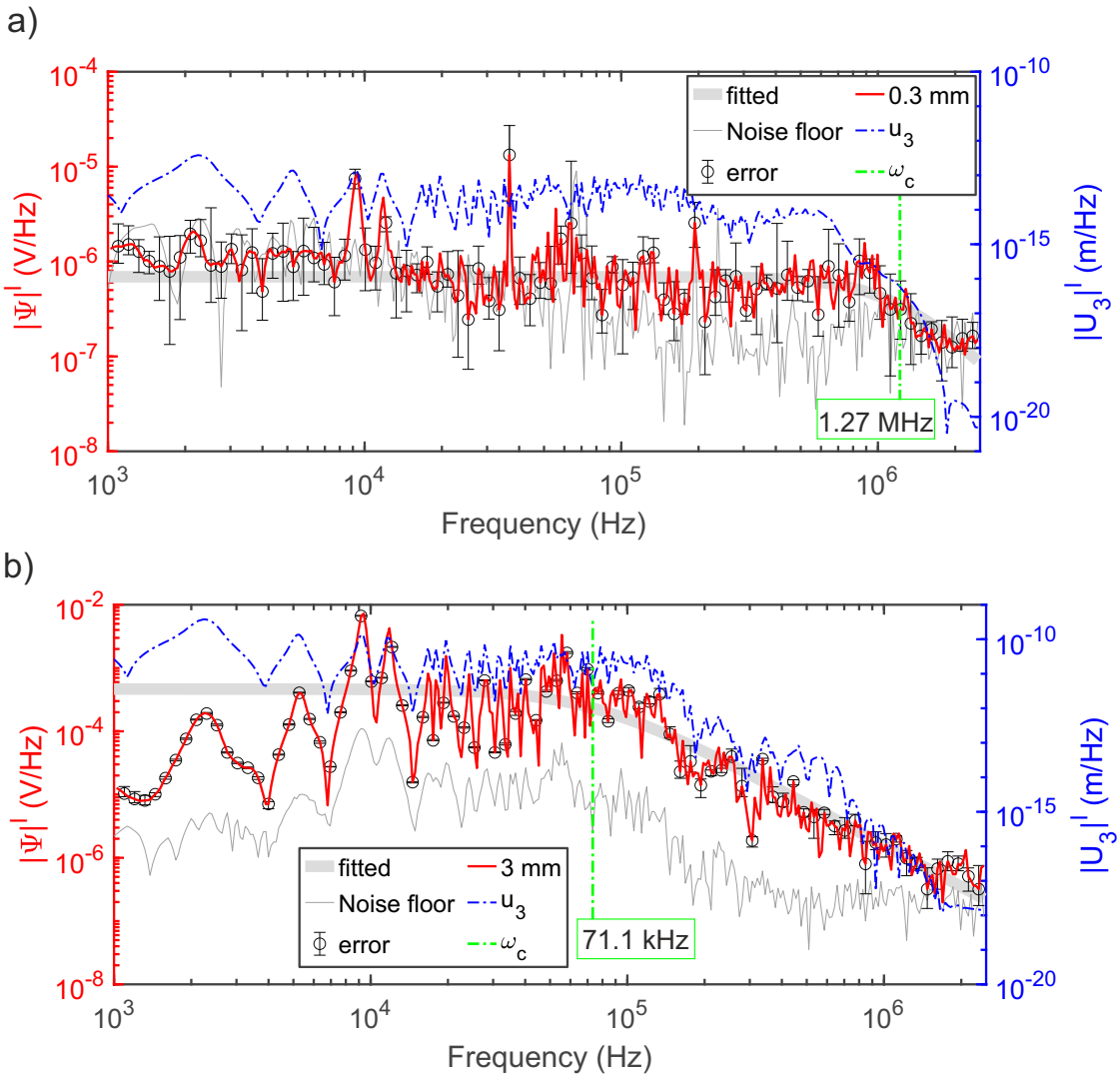

Figure 8. Amplitude spectra of voltage $|\Psi|^l$ (red line), background noise (thin gray line), *Omega-n* model (thick gray line) and displacement $|U_3|^l$ (blue line) of (a) 0.3 mm and (b) 3 mm diameter ball impacts over a long duration (8000 μs).

of $|\Psi|^l$ and 174.6 kHz and determine the valid frequency band from 1 to 71.1 kHz, where the the mean value of SNR is around 20. Both $|U_3|^l$ and $|\Psi|^l$ are relatively flat below ω_c; they have a distinct and similar spectrum shape regarding the local minima and maxima, which indicates the resonance and anti-resonance of the steel transfer plate due to the ball impact. By comparing Fig. 8(a) and (b), we find that, with the longer contact times (i.e., from 0.5 to 4.7 μs) associated with larger (i.e., from 0.3 to 3 mm) ball drops, the interaction between elastic waves and the Hertz impact force history could enhance the resonance and anti-resonance observed in the experimental data. The similarity between the experimental data

(voltage) and theoretical estimation (displacement) validates the proposed methodology for deriving low-frequency NGFs.

5 BROADBAND CHARACTERIZATION OF PZT SENSORS

In above sections, we presented the displacement $|U_3|_{\chi}^{s,l}$ and voltage $|\psi|_{\chi}^{s,l}$ in low- and high-frequency analyses of the dynamic Hertz impact problem, with a unique ball diameter label, $\chi \in [1, N]$, where N denotes the number of ball sizes. In accordance with Eq. (8), we obtain a group of segmented instrumental responses $I_{3,\chi}^{s,l}$ with different forces and durations of ball impact. In this section, we develop an algorithm to integrate a group of $I_{3,\chi}^{s,l}$ into a truly broadband understanding of I_3 from 1 kHz to 1 MHz for an array of PZT sensors.

5.1 Integrate segmented instrumental response

We are reminded of the fact that a specific member of the $I_{3,\chi}^{s,l}$ group is not valid over the whole frequency bandwidth (from 1 kHz to 1 MHz). Instead, the accuracy of $I_{3,\chi}^{s,l}$ is regulated by the quality of the experimental data (i.e., ω_c of $|\Psi|^{s,l}$, SNR) and solution accuracy of the FEM-based numerical modelling. If we perform a simple union operation of the $I_{3,\chi}^{s,l}$ group, the broadband I_3 will be distorted, with various level of uncertainty, by introducing all the components of $I_{3,\chi}^{s,l}$. To obtain a more accurate I_3, we perform several 'cropping' operations to constrain the $I_{3,\chi}^{s,l}$ group.

The solution accuracy of the modelling methodology is closely related to the mesh discretization. In high-frequency analysis, $I_{3,\chi}^{s}$ is picked from 100 kHz (the lower bound of the valid frequency band for the *f-FEM* model) to ω_c of $|\Psi|^s$ by spectrum fitting. In low-frequency analysis, $I_{3,\chi}^{l}$ is cropped from 1 kHz to the minimum between 174.6 kHz (the upper bound of the valid frequency band of the *c-FEM* model) and ω_c of $|\Psi|^l$. This *primary cropping* operation can be denoted as $/\cdots/$.

The quality of the experimental data is mainly controlled by the SNR (or ball size: large ball impacts generate higher SNR, see Section 4.2) and the repeatability of the test data. To alleviate the effect of background noise, a *secondary cropping* operation is proposed to better select the frequency band of $I_{3,\chi}^{s,l}$ based on the criterion of SNR > 1. We denote this as $\langle \cdots \rangle$. In this case, the small ball impact has a limited contribution to the broadband I_3 due to its low SNR especially at the low-frequency range. We have illustrated the repeatably of ball impact tests in Section 4, but there exists an amplitude offset of $I_{3,\chi}^{s,l}$ during repeated tests. We therefore remove the frequency band where the relative error of $|\Psi|^{s,l}$ is larger than 2 %. We then average $I_{3,\chi}^{s,l}$ over the rest of the frequency band; this *tertiary cropping* operation as $\overline{\cdots}$ is denoted.

Once the above 'cropping' operations are implemented, the $I_{3,\chi}^{s}$ group is well constrained. We now need to link all the cropped $I_{3,\chi}^{s}$ together from the low- and high-frequency analyses over a broad range of ball diameters. The final broadband I_3 is written as

$$I_3 = \sum_{\chi=1}^{N} \overline{\langle / |\, I_{3,\chi}^{l} \,| / \rangle} \cup \overline{\langle / |\, I_{3,\chi}^{s} \,| / \rangle}, \tag{17}$$

where $\cup$ is the *primary link* operation between the low- and high-frequency cases, $\sum$ denotes the *secondary link* operation over different ball diameters.

Apart from selecting the frequency bandwidth of interest, we also explore the seismic sensitivity of the PZT sensors. McLaskey et al. (2015) provided a theoretical formulation to relate the seismic moment of internal seismic sources to the change in momentum from the external ball impact sources. Here, seismic moment is estimated using the magnitude moment M_w. In Fig. 9, we present the seismic magnitude M_w versus valid frequency band of the grouped ball impacts. We find that M_w is equivalent to extremely small earthquakes ranging from -7.9 to -5.9. This suggests that after our characterization work, we should be

able to study microcrack mechanisms by investigating source parameters via radiated elastic waves, where the amount of slip could be on the order of sub-micrometer (Selvadurai 2019).

In Fig. 9, the region between ω_{χ}^{min} (black dashed line) and ω_{χ}^{max} (black solid line) suggests that these overlapped frequency bands of ball drops could fully cover the frequency scope of interest (from 1 kHz to 1 MHz). Here ω_{χ}^{min} and ω_{χ}^{max} represent the minimum and maximum valid frequencies of ball drops, respectively. We see that the results from ball impact tests with diameters of 0.3, 1 and 3 mm almost cover broadband frequency range. This provides researchers with straightforward instructions about how to choose the right parameters for ball impact tests in accordance with their frequency range of interest when performing PZT sensor characterization. Moreover, if characterization tests of PZT sensors are performed on the test platens made of brittle rocks instead of steel under same range of ball sizes, the detected M_w of ball impacts would shift to a lower bound (i.e. -8.5 to -6.5) because of the differences in material density, P- and S-wave speeds for steel and brittle rock (see Appendix from McLaskey et al. (2015)). The results can also be extended to seismic events with larger magnitude and lower frequency components, but this might require longer durations of the elastic wave propagation, larger ball sizes, larger test platens, and different digitization ranges.

5.2 Single PZT sensor: broadband I_3

In this section, we illustrate the differences in the calculated broadband instrumental response I_3 of a single PZT sensor with and without cropping algorithm (see Eq. (17)). In the lower part of Fig. 10(a), we show the original I_3^d in a marker symbol series from 1 kHz to 1 MHz (units: dB, the superscript d denotes displacement). We use 1 V/nm as the reference sensitivity of the PZT sensors to measured displacement. We see that, without cropping

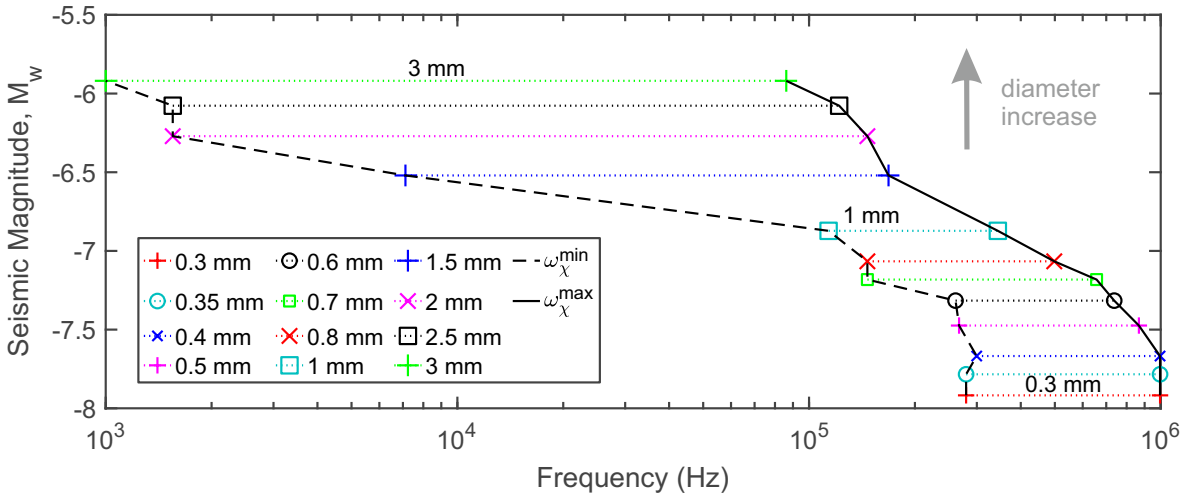

Figure 9. Seismic magnitude M_w versus valid frequency band from a series of repeated ball drop tests (marker symbols) with diameters ranging from 0.3 to 3mm.

some components from the final I_3, there are remarkable amplitude variations of I_3^d in the frequency bandwidth of 1 to 7 kHz and 14 to 170 kHz, respectively.

Following the proposed algorithm described in Eq. (17), we obtain the cropped broadband I_3^d. In the lower part of Fig. 10(b), we see that the 12 data series (for 0.3 to 3 mm ball diameters) overlap with little vertical shift. This suggests a promising stability of the developed algorithm, as well as the characterization methodology. The linked I_3^d (gray thick line) is almost flat from 10 kHz to 1 MHz with a slope of nearly 0 dB/decade and shows a strong dependence on the measured displacement. We suggest that the PZT sensors used in this study can be used as a displacement-sensitive transducer from 10 kHz to 1 MHz. In the left lower part of Fig. 10(b), from 1 to 10 kHz, the linked I_3^d has a slope of 40 dB/decade.

By performing the transformation of displacement into acceleration in the frequency domain, we rewrite the displacement-based I_3^d into the acceleration-based I_3^a as

$$I_3^a = \frac{I_3^d}{(2\pi\omega)^2}, \tag{18}$$

where the superscript a denotes acceleration. We add the original and cropped I_3^a into Fig. 10. In Fig. 10(a), that has no cropping, we find remarkable amplitude variations for the

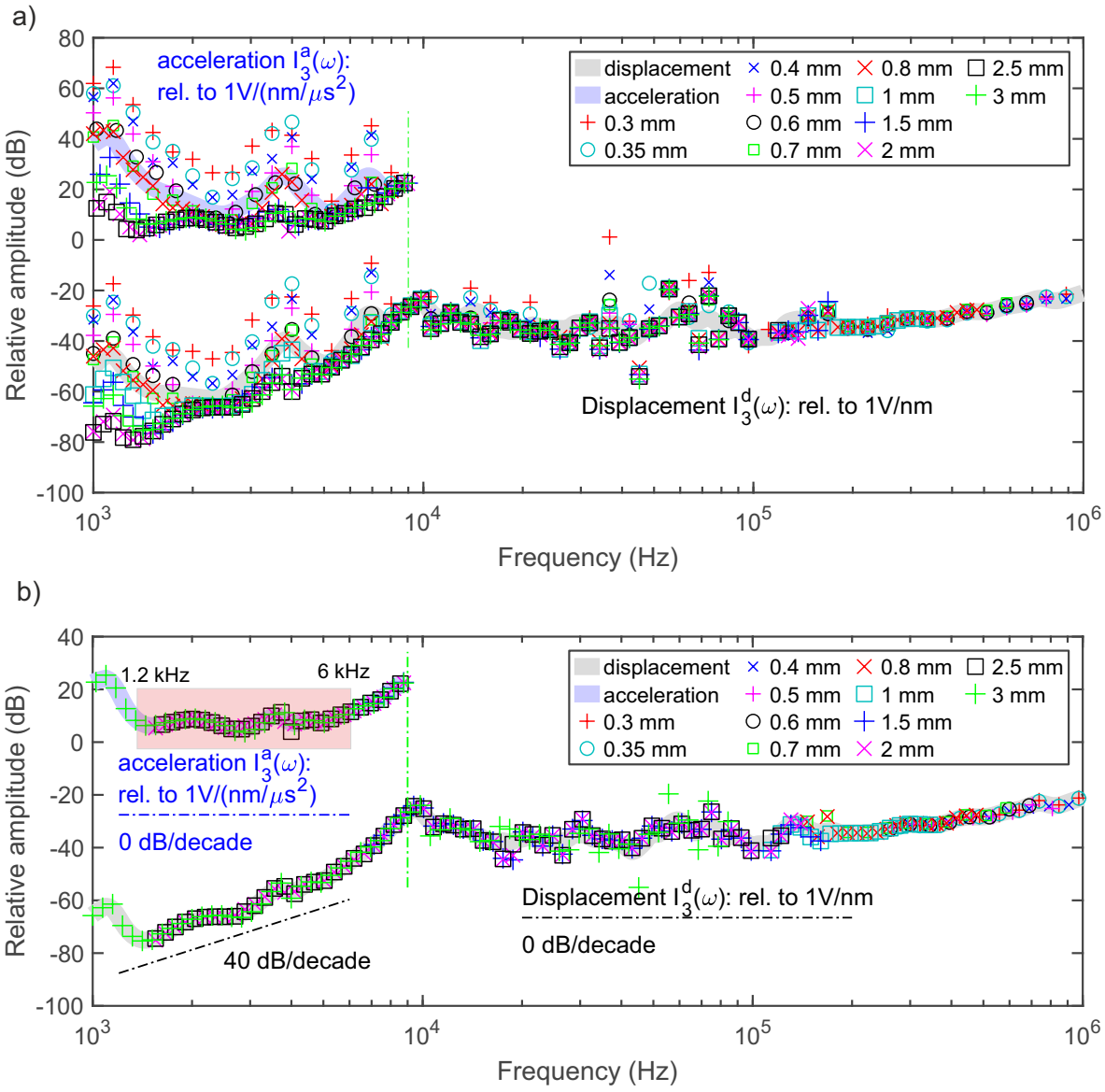

Figure 10. (a) Original and (b) cropped displacement-based (gray thick line) and acceleration-based (blue thick line) instrumental response of a single PZT sensor from a series of repeated ball drop tests (marker symbols) with diameters ranging from 0.3 to 3 mm. The cropping operations to I_3 refers to Eq. 17.

data series of I_3^a from 1 to 7 kHz. In Fig. 10(b), we find that the I_3^a segments overlap well with little vertical shift and the linked I_3^a (blue thick line in the upper part of Fig. 10(b)) is relatively flat from 1.2 to 6 kHz. The PZT sensor is sensitive to time-varying acceleration over this frequency range, where the sensor shows similar responses as accelerometers.

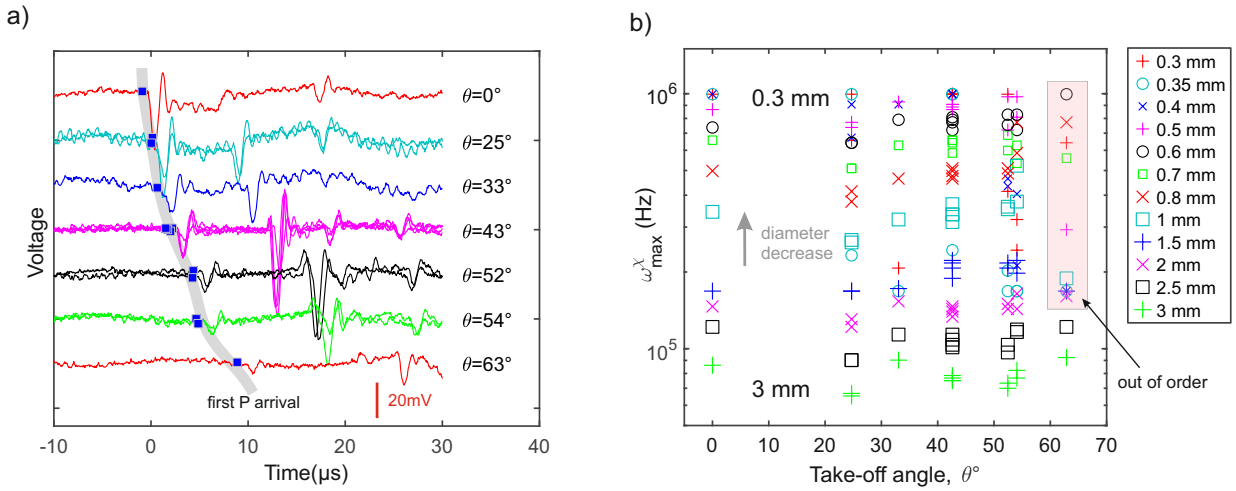

Figure 11. (a) Raw voltage signals (colored) measured by a PZT sensor array at a group of take-off angles caused by a 0.5 mm diameter ball impact. (b) The maximum valid frequency versus take-off angle with ball diameters ranging from 0.3 to 3 mm.

5.3 PZT sensor array: broadband I_3 group

We now extend the analysis of the instrumental response of a single PZT sensor to that of an array of PZT sensors of the same KRN Services model. The detailed arrangement of the PZT sensor array is given in Section 2.2.

In Fig. 11(a), we show the voltage signals near the first P-wave arrival (blue square) for all sensors, with the take-off angle ranging from 0° to 62.9° caused by a 0.5 mm diameter ball impact. At time $t = 0$, the first P-wave arrives in the ray path θ=0°. We see that the

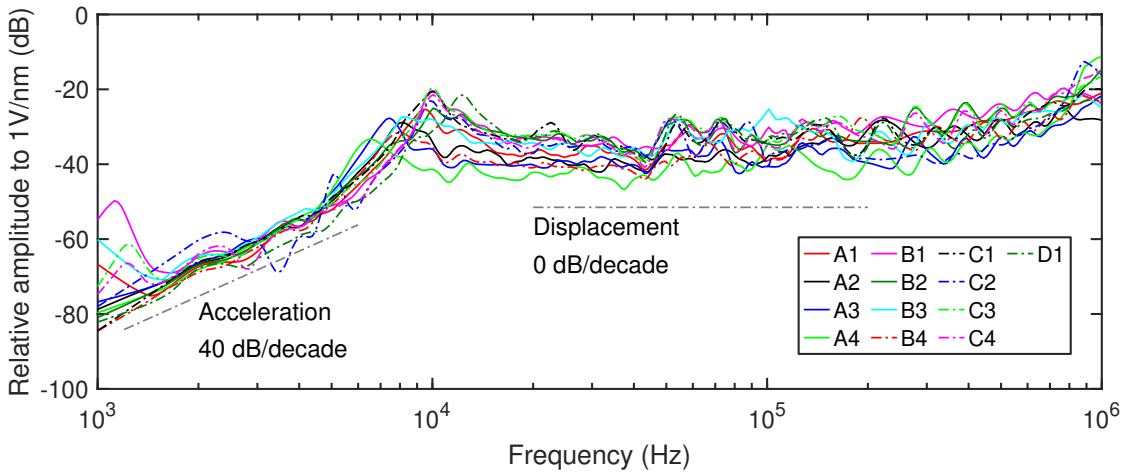

Figure 12. Summary of displacement-based instrumental responses (colored) over 13 PZT sensors. A1 to D1 represent the label given to the PZT sensors. We have shown displacement- and acceleration-dependence (gray dash dot line) of I_3^d over 10 kHz to 1 MHz and 1 to 6 kHz, respectively.

time of the first P-wave arrival has a positive dependence (gray line) on the take-off angle while the first peak amplitude of the P-wave decreases significantly as the take-off angle increases. Since there are several sensors at the same take-off angle (i.e., θ=42.6° - A3, B2, C3, C4), we find that the corresponding shape of the voltages matches well with each other. But, due to the I_3 variation at the level of uncertainty among these sensors, there exist scaling factors of the absolute amplitude of voltages. Through these observations, we suggest that the proposed experimental configuration realistically captures the elastic wave propagation phenomena using an array of PZT sensors.

We obtain a group of NGFs from all source-receiver pairs and derive the corresponding displacements. The same procedures used for characterization of a single PZT sensor are followed. By using the algorithms described in Eq. (17), we obtain the valid frequency bandwidth over a broad range of ball diameters for all PZT sensors. In Fig. 11(b), we show the ω_χ^{max} of the valid frequency bandwidth versus the take-off angle θ under ball impacts with different diameters. We find that when θ ranges from 0° to 54.0°, the ω_χ^{max} of all PZT sensors from the same ball impact has minor variations. Moreover, ω_χ^{max} has a positive dependence on the ball size. However, when θ increases to 62.9°, there is weak resultant displacement in the $\mathcal{3}$-direction measured by PZT sensor C2. The derived ω_χ^{max} group corresponding to small ball diameters ($<$ 2 mm) are out of order, suggesting that in the characterization experiments, we should keep the epicenter of PZT sensors close to the location of the ball impact. Note that we used conical shaped PZTs throughout these experiments; the corresponding analysis could be quite different for cylindrically shaped PZTs (Ono 2019).

All the PZT sensors used in this study have been used in laboratory fracturing experiments for some time (more than 3 years). Therefore they are assumed to have a similar response to mechanical vibration but are not exactly identical due to damage of the crystal material as well as uncertain variations in the manufacturing. In Fig. 12, we show well-

stacked I_3^d of all the PZT sensors from 1 kHz to 1 MHz . We see that all these PZT sensors have similar displacement- and acceleration-dependence from 10 kHz to 1 MHz and from 1 to 6 kHz, respectively.

6 CONCLUSIONS

In this study, we presented a comprehensive FEM analysis of laboratory elastic stress wave modelling to obtain accurate NGFs between an active source and an array of PZT sensors where the modelling parameters are similar to the experimental configuration. To avoid expensive computational costs on separate simulations to calculate the EGFs of a group of ball impacts, we used a unit step force-time function to describe the loading applied at the same location for the ball impacts. The resulting theoretical displacement was readily calculated by performing the convolution between the NGFs and the force-time function of the ball impacts.

We performed two separate simulations; low-frequency modelling based on a relatively coarse grid (*c-FEM*), and high-frequency modelling based on a relatively fine grid (*f-FEM*). Both models were validated against the reference approach over the high-frequency band. We performed the low-frequency analysis of wave propagation phenomena which integrated more realistic boundary conditions among the different experimental components. We suggest that the results from the *c-FEM* model have better physical foundations. Both the high-frequency validation and low-frequency extension work successfully demonstrate the capabilities of the constructed model to solve the elastic wave propagation problem.

We performed impacts tests using balls with diameters changing from 0.3 to 3 mm and obtained a group of segmented instrumental responses $I_{3,\chi}^{s,l}$ with various levels of bandwidth overlap. To obtain the broadband I_3, we developed algorithms to accurately pick the band-

width of $I^{s,l}_{3,\chi}$ by considering the solution accuracy of the modelling methodology and quality of the experimental data. We showed that, to rigorously understand the measured seismic magnitude M_w and valid frequency bandwidth of I_3, a broad range of ball diameters are needed. Finally we obtained an accurate I_3 for an array of PZT sensors at different take-off angles.

This study focused on developing methods that can bridge the gap between qualitative analysis and quantitative characterizations of laboratory and *in situ* AEs. Following the proposed methodology, we can absolutely calibrate PZT sensors and thus properly interpret the messages of ground motion from AE monitoring. In future, to study the physics of dynamic failures from near-surface to subsurface conditions, PZT sensors need to be characterized in prior under complicated conditions (i.e. sensors sit inside a pressurised, fluid filled triaxial cell at high-temperature). Our constructed models can potentially be integrated with state-of-the-art multiphysics couplings from COMSOL Multiphysics such that a well-validated FEM model capable at solving (multiphysics) problems of elastic wave propagation can be developed. We can then provide accurate insights into the source properties of microcrack behavior and quantitatively study the damage evolution and fracture propagation in brittle rocks over a broadband frequency range and source dimensions.

ACKNOWLEDGEMENT

The authors are indebted to the work and enthusiasm of Mr. Thomas. Mörgeli. He has been instrumental in the study and provided critical input, design strategy and technical expertise for the development the calibration station (Fig. 2(a)). His work is supported through the Rock Physics and Mechanics Laboratory at ETH Zurich. The authors would also like to

thank Elsys company, especially Roman Bertschi for their hardware and software support for this research. Mr. Wu is financially by China Scholarship Council (CSC, No. 201806440037).

REFERENCES

Aki, K. & Richards, P. G., 2002. *Quantitative seismology*, University Science Books.

Amann, F., Gischig, V., Evans, K., Doetsch, J., Jalali, R., Valley, B., Krietsch, H., Dutler, N., Villiger, L., Brixel, B., & others, 2018. The seismo-hydromechanical behavior during deep geothermal reservoir stimulations: open questions tackled in a decameter-scale in situ stimulation experiment, *Solid Earth*, **9**(1), 115–137.

Askey, R. A. & Roy, R., 2010. Gamma function, in *NIST Handbook of mathematical functions*, chap. 5, pp. 135–147.

Bracewell, R. N., 1986. *The Fourier transform and its applications*, vol. 31999, McGraw-Hill New York.

Breckenridge, F., Proctor, T., Hsu, N., Fick, S., & Eitzen, D., 1990. Transient sources for acoustic emission work, in *Progress in Acoustic Emission*, pp. 20–37, Japanese Society for Non-Destructive Inspection, Tokyo.

Cohen, M. & Jennings, P. C., 1983. Silent Boundary Methods for Transient Analysis, in *Computational Methods for Transient Analysis*, eds Belytschko, T. & Hughes, T., Elsevier.

COMSOL AB, 2019. COMSOL Multiphysics® v. 5.5.

Gasch, T., Malm, R., & Ansell, A., 2016. A coupled hygro-thermo-mechanical model for concrete subjected to variable environmental conditions, *International Journal of Solids and Structures*, **91**, 143–156.

Glaser, S. D., Weiss, G. G., & Johnson, L. R., 1998. Body waves recorded inside an elastic half-space by an embedded, wideband velocity sensor, *The Journal of the Acoustical Society of America*, **104**(3), 1404–1412.

Goodfellow, S. D., 2015. *Quantitative Analysis of Acoustic Emission from Rock Fracture Experiments*, Ph.D. thesis, University of Toronto (Canada).

Goodfellow, S. D. & Young, R. P., 2014. A laboratory acoustic emission experiment under in situ conditions, *Geophysical Research Letters*, **41**(10), 3422–3430.

Grigoli, F., Cesca, S., Priolo, E., Rinaldi, A. P., Clinton, J. F., Stabile, T. A., Dost, B., Fernandez,

M. G., Wiemer, S., & Dahm, T., 2017. Current challenges in monitoring, discrimination, and management of induced seismicity related to underground industrial activities: A European perspective, *Reviews of Geophysics*, **55**(2), 310–340.

Grosse, C. U. & Ohtsu, M., 2008. *Acoustic emission testing*, Springer Science & Business Media.

Hanks, T. C., 1979. b values and $\omega\gamma$ seismic source models: Implications for tectonic stress variations along active crustal fault zones and the estimation of high-frequency strong ground motion, *Journal of Geophysical Research: Solid Earth*, **84**(B5), 2235–2242.

Hsu, N. N., 1985. Dynamic Green's functions of an infinite plate-A computer program, Tech. rep., National Bureau of Standards, Center for Manufacturing Engineering, Gaithersburg.

Ishida, T., Labuz, J. F., Manthei, G., Meredith, P. G., Nasseri, M. H. B., Shin, K., Yokoyama, T., & Zang, A., 2017. ISRM suggested method for laboratory acoustic emission monitoring, *Rock Mechanics and Rock Engineering*, **50**(3), 665–674.

Johnson, L. R., 1974. Green's function for Lamb's problem, *Geophysical Journal International*, **37**(1), 99–131.

Kneafsey, T. J., Dobson, P., Blankenship, D., Morris, J., Knox, H., Schwering, P., White, M., Doe, T., Roggenthen, W., Mattson, E., & others, 2018. An overview of the EGS Collab project: field validation of coupled process modeling of fracturing and fluid flow at the Sanford Underground Research Facility, Lead, SD, in *43rd Workshop on Geothermal Reservoir Engineering, Stanford University, paper SGP-TR-213. Preprint at, https://pangea. stanford. edu/ERE/pdf/IGAstandard/SGW/2018/Kneafsey. pdf*.

Kwiatek, G., Plenkers, K., Dresen, G., & Group, J. R., 2011. Source parameters of picoseismicity recorded at Mponeng Deep Gold Mine, South Africa: Implications for Scaling Relations, *Bulletin of the Seismological Society of America*, **101**(6), 2592–2608.

Kwiatek, G., Plenkers, K., Martínez-Garzón, P., Leonhardt, M., Zang, A., & Dresen, G., 2017. New insights into fracture process through in-situ acoustic emission monitoring during fatigue hydraulic fracture experiment in Äspö Hard Rock Laboratory, *Procedia Engineering*, **191**, 618–622.

Lamb, H., 1904. On the propagation of tremors over the surface of an elastic solid, *Philosophical Transactions of the Royal Society of London. Series A, Containing papers of a mathematical or physical character*, **203**(359-371), 1–42.

Lockner, D., 1993. The role of acoustic emission in the study of rock fracture, *International*

Journal of Rock Mechanics and Mining Sciences & Geomechanics Abstracts, **30**(7), 883–899.

Manthei, G. & Plenkers, K., 2018. Review on in situ acoustic emission monitoring in the context of structural health monitoring in mines, *Applied Sciences*, **8**(9), 1595.

McLaskey, G. C. & Glaser, S. D., 2010. Hertzian impact: Experimental study of the force pulse and resulting stress waves, *The Journal of the Acoustical Society of America*, **128**(3), 1087–1096.

McLaskey, G. C. & Glaser, S. D., 2011. Micromechanics of asperity rupture during laboratory stick slip experiments, *Geophysical Research Letters*, **38**(12).

McLaskey, G. C. & Glaser, S. D., 2012. Acoustic emission sensor calibration for absolute source measurements, *Journal of Nondestructive Evaluation*, **31**(2), 157–168.

McLaskey, G. C., Kilgore, B. D., Lockner, D. A., & Beeler, N. M., 2014. Laboratory generated M -6 earthquakes, *Pure and Applied Geophysics*, **171**(10), 2601–2615.

McLaskey, G. C., Lockner, D. A., Kilgore, B. D., & Beeler, N. M., 2015. A robust calibration technique for acoustic emission systems based on momentum transfer from a ball drop, *Bulletin of the Seismological Society of America*, **105**(1), 257–271.

Moradian, Z., Einstein, H. H., & Ballivy, G., 2016. Detection of cracking levels in brittle rocks by parametric analysis of the acoustic emission signals, *Rock Mechanics and Rock Engineering*, **49**(3), 785–800.

Ono, K., 2019. Rayleigh wave calibration of acoustic emission sensors and ultrasonic transducers, *Sensors (Switzerland)*, **19**(14), 3129.

Pao, Y. & Gajewski, R. R., 1977. The generalized ray theory and transient responses of layered elastic solids, *Physical Acoustics*, **13**, 183–265.

Reed, J., 1985. Energy losses due to elastic wave propagation during an elastic impact, *Journal of Physics D: Applied Physics*, **18**(12), 2329–2337.

Schnabel, S., Golling, S., Marklund, P., & Larsson, R., 2017. Absolute measurement of elastic waves excited by Hertzian contacts in boundary restricted systems, *Tribology Letters*, **65**(1), 1–11.

Schoenball, M., Ajo-Franklin, J., Blankenship, D., Cook, P., Dobson, P., Guglielmi, Y., Fu, P., Kneafsey, T., Knox, H., Petrov, P., & others, 2019. Microseismic monitoring of meso-scale stimulations for the DOE EGS Collab project at the Sanford Underground Research Facility, in *Proceedings: 44th Workshop on Geothermal Reservoir Engineering, Stanford University, Stanford, CA*.

Selvadurai, A. P. S. & Najari, M., 2013. On the interpretation of hydraulic pulse tests on rock specimens, *Advances in Water Resources*, **53**, 139–149.

Selvadurai, A. P. S. & Najari, M., 2017. The thermo-hydro-mechanical behavior of the argillaceous Cobourg Limestone, *Journal of Geophysical Research: Solid Earth*, **122**(6), 4157–4171.

Selvadurai, A. P. S. & Suvorov, A. P., 2017. *Thermo-Poroelasticity and Geomechanics*, Cambridge University Press, Cambridge.

Selvadurai, A. P. S., Suvorov, A. P., & Selvadurai, P. A., 2015. Thermo-hydro-mechanical processes in fractured rock formations during a glacial advance, *Geoscientific Model Development*, **8**(7), 2167–2185.

Selvadurai, P. A., 2019. Laboratory insight into seismic estimates of energy partitioning during dynamic rupture: An observable scaling breakdown, *Journal of Geophysical Research: Solid Earth*, **124**, 11350–11379.

Selvadurai, P. A. & Selvadurai, A. P. S., 2014. On the effective permeability of a heterogeneous porous medium: the role of the geometric mean, *Philosophical Magazine*, **94**(20), 2318–2338.

Villiger, L., Gischig, V. S., Doetsch, J., Krietsch, H., Dutler, N. O., Jalali, M., Valley, B., Selvadurai, P. A., Mignan, A., Plenkers, K., Giardini, D., Amann, F., & Wiemer, S., 2020. Influence of reservoir geology on seismic response during decameter-scale hydraulic stimulations in crystalline rock, *Solid Earth*, **11**(2), 627–655.

Wu, B. S. & McLaskey, G. C., 2018. Broadband calibration of acoustic emission and ultrasonic sensors from generalized ray theory and finite element models, *Journal of Nondestructive Evaluation*, **37**(1), 8.

Wu, B. S. & McLaskey, G. C., 2019. Contained Laboratory Earthquakes Ranging from Slow to Fast, *Journal of Geophysical Research: Solid Earth*, **124**(10), 10270–10291.

Ye, R., de Hoop, M. V., Petrovitch, C. L., Pyrak-Nolte, L. J., & Wilcox, L. C., 2016. A discontinuous Galerkin method with a modified penalty flux for the propagation and scattering of acousto-elastic waves, *Geophysical Journal International*, **205**(2), 1267–1289.

Zang, A., Stephansson, O., Stenberg, L., Plenkers, K., Specht, S., Milkereit, C., Schill, E., Kwiatek, G., Dresen, G., Zimmermann, G., Dahm, T., & Weber, M., 2016. Hydraulic fracture monitoring in hard rock at 410 m depth with an advanced fluid-injection protocol and extensive sensor array, *Geophysical Journal International*, **208**(2), 790–813.

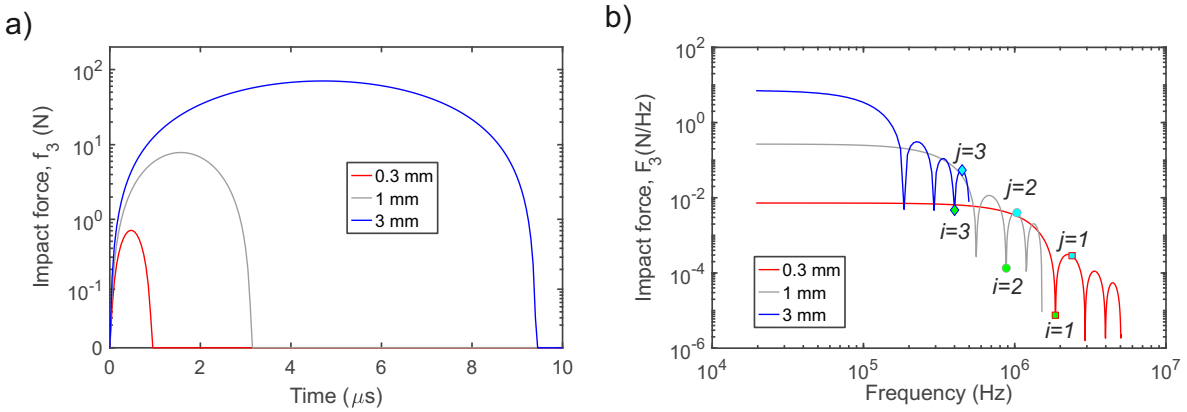

Figure A1. (a) Force-time function, $f_3(t)$, and (b) its amplitude spectrum, $F_3(\omega)$. For visualization, $f_3(t)$ and $F_3(\omega)$ with diameters of 0.3 mm (red), 1 mm (gray) and 3 mm (blue) are displayed.

APPENDIX A: HERTZIAN IMPACT SOURCE

We used spherical ball impacts as the mechanical active source to excite stress waves in our transfer plate. In Fig. A1(a), when the steel ball instantaneously impacts the steel transfer plate, the force-time function $f_3(t)$ derived from the Hertzian impact theory (Reed 1985) can be written as

$$\begin{aligned} f_3(t) &= f_{\max} \sin\left(\frac{\pi t}{t_c}\right)^{\frac{3}{2}}, 0 < t \leq t_c, \\ f_3(t) &= 0, t > t_c, \end{aligned} \tag{A.1}$$

where $f_{max} = 1.917\rho_1^{3/5}\left(\delta_1+\delta_2\right)^{-2/5} R_1^2 v_0^{6/5}$ denotes the maximum force of the ball impact, and $t_c = 4.53\left(4\rho_1\pi\left(\delta_1+\delta_2\right)/3\right)^{2/5} R_1 v_0^{-1/5}$ is the contact time between the ball and test specimen. R_1 and ρ_1 are the ball radius and density, respectively. δ_i is a material constant depending on Young's modulus, E_i, and Poisson's ratio, μ_i, of the ball and the plate, that is $\delta_i = (1-\mu_i^2)/(\pi E_i), i = 1, 2$. $v_0 = \sqrt{2gh_d}$ represents the impact velocity due to the free drop motion, where h_d and g are the dropping height and gravitational acceleration, respectively.

The amplitude spectrum of $f_3(t)$, denoted by $F_3(\omega)$, is expressed as

$$F_3(\omega) = 0.2689 \frac{\Delta P}{\Gamma\left(\frac{7}{4} + t_c\omega\right) \left|\Gamma\left(\frac{7}{4} - t_c\omega\right)\right|}, \tag{A.2}$$

where $\Delta P \approx 0.5564(t_c f_{\max})$ is the change in momentum that the ball imparts to the steel transfer plate. Γ is the Gamma function (Askey & Roy 2010).

Due to the properties of $\Gamma(z)$ at non-positive integers, there exists a group of local minima and maxima of $F_3(\omega)$, where

$$\begin{aligned} &\frac{7}{4} - t_c\omega_0 = 0, -1, -2, ..., -i \Rightarrow \omega_0^i = \frac{i + \frac{7}{4}}{t_c}, \\ &\frac{7}{4} - t_c\omega_p = -\frac{1}{2}, -\frac{3}{2}, ..., -\frac{2j+1}{2} \Rightarrow \omega_p^j = \frac{j + \frac{9}{4}}{t_c}. \end{aligned} \tag{A.3}$$

Here i, j are non-negative integers. ω_0^i and ω_p^j are the frequency group corresponding to the local minima $F_3(\omega_0^i)$ of the i th and local maxima $F_3(\omega_p^j)$ of the j th lobe of $F_3(\omega)$. ω_0^i is also termed the "zero frequency" (McLaskey & Glaser 2010). Fig. A1(b) illustrates this. When $F_3(\omega)$ deviates from a flat plateau, spectral energy attenuates rapidly with changes of 2 to 3 orders of magnitude, from 100 kHz to 1 MHz for the force-time function of the 1 mm diameter ball impact (grey lines). The marker symbols positioned by ω_0^i and ω_p^j show the separation of a series of lobes in the spectral energy falloff phase. These characteristics of a series of lobes are useful to validate the theoretical $f_3(t)$ against the calibration at experimental data discussed in Section 4.1.